TECHNISCHE UNIVERSITÄT WIEN
Vienna | Austria

MASTER THESIS

A multiple-resolution strategy for two-phase flow simulations using the Phase Field Method

carried out for the purpose of obtaining the degree of Master of Science,

submitted at TU Wien, Faculty of Mechanical and Industrial Engineering, by

Maximilian Schenk

Mat.Nr.: 01526410

BOARD MEMBERS

Prof. Alfredo Soldati	SUPERVISOR
Dr. Francesco Zonta	CO-SUPERVISOR
George Giamagas, M.Sc.	CO-SUPERVISOR

Vienna, October 2022

Author's e-mail:

maximilianschenk@outlook.com

Author's address:

Institute of Fluid Mechanics and Heat Transfer, E322

Vienna University of Technology

Tower BA/E322, Getreidemarkt 9

1060 Vienna – Austria

Cover:

Shape of the interface between two fluids after $t^+ = 80$. Second fluid is is centered in the main fluid. Turbulent multiphase flow.

Acknowledgments

First and foremost, I would like to thank my supervisor, Mr. Prof. Alfredo Soldati, and my co-supervisor, Mr. Dr. Francesco Zonta, for making this work possible under their supervision. Furthermore, I would also like to thank my co-supervisor, Mr. George Giamagas M.Sc., for his continuous encouragement and helpful guidance throughout my work. It should also be mentioned how fortunate I was for the endless discussions and for the forthwith responses to my questions and queries from this trio.

Last but not least, I am really grateful to my mother, Iris Schenk, and my step-father, Markus Forster, for their endless support and patience with me throughout my career. It should be mentioned that my career would not have happened without you. I just want to say thank you for everything!

Abstract

In this work, a multiple-grid Phase Field Method PFM approach has been implemented using a Direct Numerical Simulation DNS. The Continuity equation CE and the Navier-Stokes equations NSE are coupled with second-order Phase Field Method PFM, where one equation is responsible for the description of the interfacial dynamics (Cahn-Hillard equation CHE) and the other one for the surfactant (Cahn-Hillard-like equation), which will not be covered in this thesis, since the mutliple-grid for the surfactant is already implemented. In the turbulence-interface model just the equation for the interface will be expanded and it is validated through two sets of benchmarks. First, a 2D benchmark is completed, where a 2D droplet is exposed in a laminar shear flow. From analytical results and previous numerical and experimental works it is known that a steady-state will be reached after some point. Therefore, the deformation and the steady-state angle will be compared for different viscosity ratios and capillary numbers. Furthermore, a 3D benchmark is obtained. A thin sheet layer is placed in the center of a turbulent channel flow and the breakage and coalescence of this thin sheet layer will be compared to the current internal code, where no expansion for the phase-field is included. Last but not least, a simulation is obtained, where the influence of different grid-resolutions on the mass leakages and the surface area development are compared.

Zusammenfassung

In dieser Arbeit wurde ein Mehrfachgitter-Phasenfeld-Methoden PFM Ansatz unter Verwendung einer Direkten Numerischen Simulation DNS implementiert. Die Kontinuitätsgleichung CE und die Navier-Stokes-Gleichungen NSE werden mit der Phasenfeldmethode PFM zweiter Ordnung gekoppelt, wobei eine Gleichung für die Beschreibung der Grenzflächendynamik (Cahn-Hillard-Gleichung CHE) und die andere für das Tensid (Cahn-Hillard-ähnliche Gleichung) zuständig ist, die in dieser Arbeit nicht behandelt wird, da das Mehrfachgitter für das Tensid bereits implementiert ist. Im Turbulenz-Grenzflächenmodell wird nur die Gleichung für die Grenzfläche erweitert und durch zwei verschiedene Benchmarks validiert. Zunächst wird ein 2D-Benchmark durchgeführt, bei dem ein 2D-Tropfen in einer laminaren Scherströmung ausgesetzt wird. Aus analytischen Ergebnissen und früheren numerischen und experimentellen Arbeiten ist bekannt, dass nach einem bestimmten Punkt ein stationärer Zustand erreicht wird. Daher werden die Verformung und der stationäre Winkel für verschiedene Viskositätsverhältnisse und Kapillarzahlen verglichen. Weiters wird ein 3D-Benchmark durchgeführt. Eine dünne Schicht wird in der Mitte einer turbulenten Kanalsträmung platziert, und das Auseinanderbrechen und das Zusammenwachsen dieser dünnen Schicht wird mit dem aktuellen internen Code verglichen, der keine Expansion des Phasenfelds enthält. Zu guter Letzt wird eine Simulation durchgeführt, bei der der Einfluss verschiedener Gitterauflösungen auf die Massenverluste und die Oberflächenentwicklung verglichen wird.

Contents

1

Introduction

Turbulent multiphase flows are of crucial importance and frequently occur in our daily life in a large number of industrial and environmental phenomena. All of these systems include gas-liquid or liquid-liquid mixtures and therefore the behavior of the system can change dramatically if it is compared to a single phase turbulent flow. In order model flows of multiple fluids of different thermophysical properties, a so-called phase-field is introduced. The model allows for accurate representation of surface tension phenomena, as well as the influence of so-called surfactants, which are substances used to reduce surface tension. For a multiphase flow, the Continuity equation and the Navier-Stokes equations are coupled with an equation for the phase-field (Cahn-Hillard equation) and an additionial equation for the surfactant (Cahn-Hillard-like equation - Surfactant is only mentioned for the sake of completeness, but is not studied during the entire work and is therefore not taken into account). This approach is based on the Phase Field Method PFM. One of the biggest downsides of the method is that it is non-mass conserving, if the Cahn-Hillard equation for the phase-field is not computed on the molecular scale $\mathcal{O}(-8)$[1]. On the contrary, if there is a turbulent flow, the Navier-Stokes equations must be resolved only down to the Kolmogorov scale $\mathcal{O}(-3)$[2], which is the smallest length scale of a turbulent flow. To get rid of this drawback, the Navier-Stokes equations must be overresolved by an order of $\mathcal{O}(5)$[3], which is considering the non-linearity and complexity of the equations is an unimaginably enormous task. To overcome this almost unsolvable problem, a dual-grid or even multiple-grid can be introduced, where the momentum equations, in particular the Navier-Stokes equations, are resolved down to the Kolmogorov length scale and the Cahn-Hillard equation for the phase-field is

[1] Compare to [32], page 3, fig.2
[2] See footnote 1
[3] See footnote 1

solved on a subgrid, which has a larger number of points along the streamwise x-, the spanwise y- and the wall-normal z-direction. In the implemented code, mutliple-grids with expansion factors (2,3,4,5, ...) are possible. In other words, this code is capable of calculating the different equations on different grids and finding a combined solution. The capability of not overresolving the Navier-Stokes equations, meanwhile the Cahn-Hillard is resolved as fine as one needs, also brings other tremendous advantages, like a lot of time, memory and disk space can be saved although no compromises in the result are to be expected.

This introduced method has another benefit; The scalar equation, namely the Cahn-Hillard equation, does not contain a pressure term compared to the Navier-Stokes equations, which means that there are still a lot of intense steep fronts. The pressure term itself makes the dynamics non-local and smoothes the intense steep fronts, normally. Thus, the phase-field contains much steeper gradients, which need to be correctly resolved and therefore a higher-resolved grid is highly recommended to describe these gradients in a correct way. [4]

[4] Compare to [23], page 3

2

Methodology

Reproduced in parts and based on:

A. Roccon. *Direct numerical simulation of turbulence-interface interactions.* University of Udine, 2017. Chapter 1. Methodology.

and

G. Soligo, *Numerical simulations of breakage, coalescence and droplet size distribution*, Vienna University of Technology, 2020. Chapter 2. Methodology.

2.1 Interfacial flow methods

2.1.1 Introduction

Interfacial flow methods can be categorized in interface tracking methods and interface capturing methods. The most popular interface tracking methods are the Front-Tracking (FT) method [10, 22], the Boundary Integral Method (BIM) [9, 33] and the Immersed Boundary Method (IBM) [17, 20]. They all have in common that they use a separated grid or mesh to track the interface, usually offer good accuracy, and require complex algorithms to handle topological changes. Interface-capturing methods use an indicator function that implicitly represents the interface on a Eulerian grid. This indicator function simplifies the handling of topological changes because a discretization is much easier to do. Common techniques are the Volume-Of-Fluid (VOF) [11, 24], the Level-Set (LS) [28, 38] and the Phase Field Method (PFM), which will be discussed in detail in the following chapter.

2.1.2 Phase Field Model

The Phase Field Method (PFM) is a diffusive interface model and was introduced by [6–8]. It was initially used to analyze the time evolution of the alloy microstructure during the spinodal decomposition. Later, this method has been extended to incompressible multiphase flows by adding an advection term and coupling it with the Navier-Stokes equations [1, 14]. The scalar order parameter ϕ describes the dynamics of the interface and corresponds to the local concentration of one of the phases. It is uniform in the bulk of the two phases and changes smoothly across the interfacial transition layer. After the advection term is added ($\mathbf{u} \cdot (\nabla \square)$ to the LHS of the Cahn-Hillard equation, one obtains ($\tilde{\cdot}$ corresponds to a dimensional variable):

$$\frac{\partial \tilde{\phi}}{\partial t} + \tilde{\mathbf{u}} \cdot \nabla \tilde{\phi} = \nabla \cdot (\tilde{\mathcal{M}}_\phi \nabla \tilde{\mu}_\phi) \tag{2.1}$$

The diffusive term on the RHS is described by the mobility parameter $\mathcal{M}_\phi$, also called the Onsager coefficient, which drives the relaxation of the interface and is assumed here to be constant. The chemical potential μ_ϕ can be obtained as the variational derivative of a Ginzburg-Landau free energy functional $\mathcal{F}[\phi, \nabla\phi]$ [3, 14, 36] and is already non-dimensionalised (for interested readers of the dimensionalised form, see [31]):

$$\mu_\phi = \frac{\partial \mathcal{F}[\phi, \nabla\phi]}{\partial \phi} \tag{2.2}$$

If we consider a system of two incompressible fluids, the function $\mathcal{F}$ is assembled by the sum of two different parts f_0 and f_i:

$$\mathcal{F}[\phi, \nabla\phi] = \int_\Omega f_\phi(\phi, \nabla\phi) d\Omega = \int_\Omega (f_0(\phi) + f_i(\nabla\phi)) d\Omega \tag{2.3}$$

Here, Ω is considered as the domain, f_0 is the bulk energy and f_i is the free mixing energy, indicating how much energy is stored within the interfacial layer.
If we use a double-well potential (2.1a) for $f_0(\phi)$ (2.4), then the physical meaning of the equation emerges, as the bulk energy $f_0(\phi)$ (2.4) favors a complete separation of the phases. The sharp-interface picture is reproduced through this 'phobic' effect. The 'philic' effect in form of the gradient term ($f_i(\nabla\phi)$ (2.5)) represents the mixing part.

These two effects interact with each other and end in the profile ϕ.[1]

For a liquid-liquid or liquid-gas layer, the mixing free energy f_i is the surface tension. The energies f_0 and f_i are defined as follows:

$$f_0(\phi) = \frac{1}{4}\Big(\phi - 1\Big)^2\Big(\phi + 1\Big)^2 \tag{2.4}$$

$$f_i(\nabla\phi) = \frac{Ch^2}{2}|\nabla\phi|^2 \tag{2.5}$$

The Cahn number $Ch = \epsilon/h$ is a non-dimensional number, which describes the ratio of the interface thickness ϵ and the length scale of the problem (half channel height h here). Taking the variational derivative of equation (2.1) gives:

$$\mu_\phi = \frac{\partial\mathcal{F}[\phi, \nabla\phi]}{\partial\phi} = \phi^3 - \phi - Ch^2\nabla^2\phi \tag{2.6}$$

At equilibrium, the chemical potential is constant throughout the domain:

$$\mu_\phi = \phi^3 - \phi - Ch^2\nabla^2\phi = \text{const.} \tag{2.7}$$

To find the equilibrium profile for ϕ (planar interface at x=0) now, one can impose $\nabla\mu_\phi = 0$ and obtain the equilibrium profile for a flat interface.

$$\phi_e = \tanh\Big(\frac{s}{\sqrt{2}Ch}\Big), \tag{2.8}$$

where s is the normal coordinate of the interface and $\phi = \pm 1$ are the values of ϕ in the bulk of the two phases. The value $\phi = -1$ decribes the carrier phase and $\phi = -1$ as the dispersed phase. In figure (2.1b), the equilibrium solution is plotted and one can obtain that in the bulk of the phases it is constant and that there is a smooth transition across the interface. The transition itself is a hyperbolic tangent profile and the thickness is proportional to the Cahn number Ch. The interfacial transition layer always needs four grid points to be represented correctly, hence, if the grid of the phase-field is condensed, the Cahn number Ch can be reduced and the smaller the Cahn number Ch, the thinner the profile of the interface gets and therefore converges to the sharp interface, as shown in figure (2.1c).

[1] Compare to [39], page 296

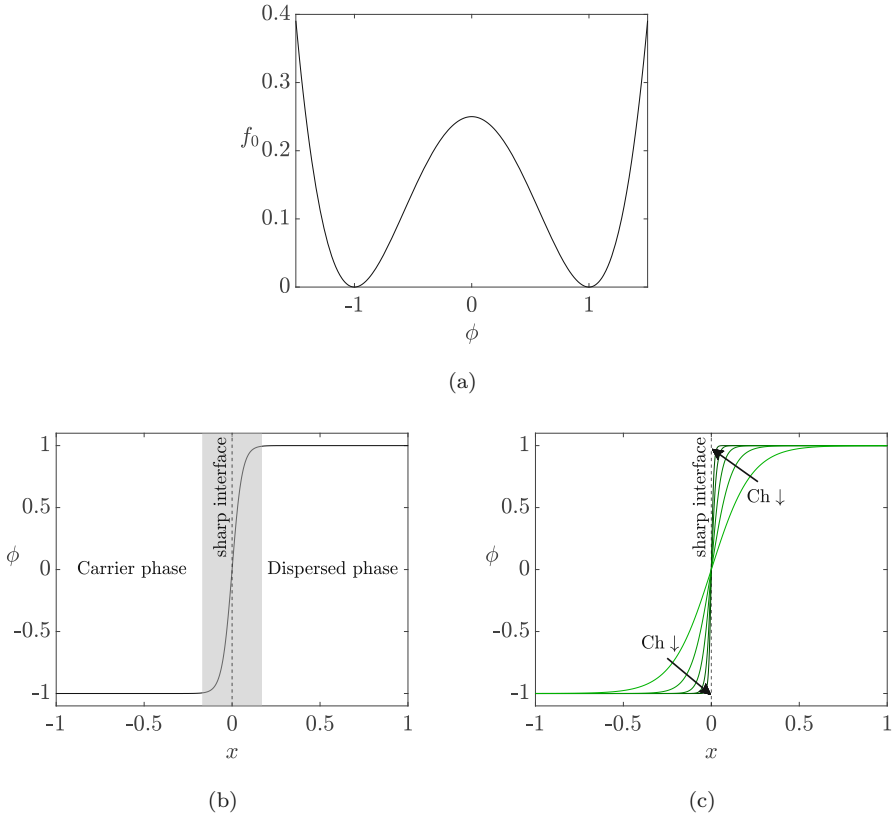

Figure 2.1 – Plot (a): Term $f_0 \rightarrow$ Double-well potential f_0. Plot (b): Equilibrium profile for a plane interface (x=0), where the dashed line indicates a sharp interface and the gray area indicates the interfacial transition layer. Plot (c): While the Cahn number Ch increases, the interfacial transition layer will get closer to the sharp interface.

The Phase Field Method has a strong physical background and is a natural extension of the Van der Waals theory of critical phenomena [37] and its thermodynamic derivation. Hence, it is capable of handling complex rheology of microstructered fluids. The structure of the interface is specified by molecular forces and when the capillary width[2] approaches zero, the diffusive-interface model reduces to the sharp-interface model (shown in (2.1b)). An additional advantage over interface-regulating methods (VOF, LS) is its energy conserving, which is shown by [19].[3]

Further advantages are that it is capable of implicit handling breakage and coalescence phenomena automatically and the accurate description of the interface. Some drawbacks of the PFM are coarsening and the incorrect representation of surface forces and thermophysical properties. However, the main drawback is its non-mass conversation and its small mass leakages, as already mentioned in the chapter (§1).

[2]Capillary width = interface thickness ϵ
[3]Compare to [39], page 295

2.2 Governing equations

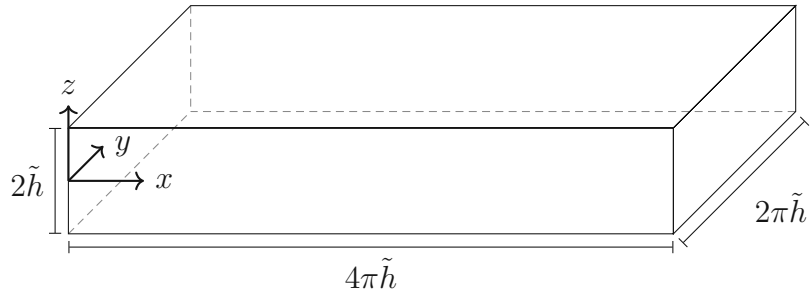

Figure 2.2 – Channel geometry used in the simulations. The channel is periodic in x- and y-directions and has respective lengths $\tilde{L}_x = 4\pi\tilde{h}$ and $\tilde{L}_y = 2\pi\tilde{h}$. Two walls are present along the z-axis and thus along the the wall-normal direction with a length in between of $\tilde{L}_z = 2\tilde{h}$

2.2.1 Flow field

There are two main approaches to solving a multiphase flow. When the sharp approach is considered, a Navier-Stokes equations for each of the phases has to be solved and to combine these two solutions appropriate boundary conditions must be applied[4]. The velocity fields $\mathbf{u_1} = (u_1\ v_1\ w_1)^T$ and $\mathbf{u_2} = (u_2\ v_2\ w_2)^T$ must satisfy the following:

$$\mathbf{u_1} \cdot \mathbf{n} - \mathbf{u_2} \cdot \mathbf{n} = 0 \tag{2.9}$$

Here, $\mathbf{n}$ is just the normal vector to the interface. Equation (2.9) describes the continuity of the velocity across the interface. A related equation must be fulfilled by the stresses:

$$\mathbf{T_1} \cdot \mathbf{n} - \mathbf{T_2} \cdot \mathbf{n} = \mathcal{K}\sigma\mathbf{n} - \nabla_s\sigma \tag{2.10}$$

Here, $\mathbf{T_1}$ and $\mathbf{T_2}$ are the stress tensors for each of the phases at the interface; $\mathcal{K}$ is the mean curvature; ∇_s is the surface gradient operator and σ is the surface tension. The first term on the RHS, $\mathcal{K}\sigma\mathbf{n}$, is the normal component and the last term on the RHS, $\nabla_s\sigma$, is the tangential one of the stress jump, which vanishes if the surface tension is uniform.

The other approach is called the continuous approach, where, of course, the same boundary conditions must be satisfied. To achieve this, not two Navier-Stokes equations

[4]Compare to [4], page 60 f.

are solved, instead there is only one Navier-Stokes equations which has to be solved for the whole domain and the boundary conditions constrain a new source term on the RHS of the equation, which takes account for the surface tension between the two phases.

2.2.2 Dimensional analysis

The governing equations in the next chapter are already non-dimensional. To do that properly, one first needs to know the way in which all variables are made dimensionless ($\tilde{\cdot}$ corresponds to a dimensional variable):

$$\mathbf{x} = \frac{\tilde{\mathbf{x}}}{\tilde{h}} \quad t = \frac{\tilde{t}\tilde{u}_\tau}{\tilde{h}} \quad \mathbf{u} = \frac{\tilde{\mathbf{u}}}{\tilde{u}_\tau} \quad \phi = \frac{\phi}{\phi_e} \quad p = \frac{\tilde{p}\tilde{h}}{\tilde{\rho}\tilde{u}_\tau^2} \quad \rho(\phi) = \frac{\tilde{\rho}(\phi)}{\tilde{\rho}_c} \quad \eta(\phi) = \frac{\tilde{\eta}(\phi)}{\tilde{\eta}_c} \tag{2.11}$$

Here, $\tilde{u}_\tau$ is the friction velocity, defined as $\tilde{u}_\tau = \sqrt{\tilde{\tau}_\omega/\tilde{\rho}}$, where $\tilde{\tau}_\omega$ is the shear stress on the wall and $\tilde{\rho}$ the density of the two phases; ϕ_e is the value assumed by ϕ in the bulk and is defined as in equation (2.8); $\tilde{\rho}_c$ and $\tilde{\eta}_c$ are the density/viscosity of the phase ($\phi = -1$) and h is the half height of the channel.

2.2.3 Summary of equations

This section summarizes the equations to be solved. Here, they are already in non-dimensional form; for interested readers in the dimensional form, see [26, 30].

$$\nabla \cdot \mathbf{u} = 0 \tag{2.12}$$

$$\rho(\phi)\frac{\partial \mathbf{u}}{\partial t} + \rho(\phi)\Big(\mathbf{u}\cdot\nabla\mathbf{u}\Big) = -\nabla p + \frac{1}{Re_\tau}\nabla\cdot\Big(\eta(\phi)(\nabla\mathbf{u} + \nabla\mathbf{u}^T)\Big) + \frac{\rho(\phi)\mathbf{g}}{Fr^2} + \underbrace{\frac{3}{\sqrt{8}}\frac{Ch}{We}\nabla\cdot[\bar{\tau}_c f_\sigma(\psi)]}_{\text{Surface tension term}} \tag{2.13}$$

$$\frac{\partial \phi}{\partial t} + \mathbf{u}\cdot\nabla\phi = \frac{1}{Pe_\phi}\nabla^2(\phi^3 - \phi - Ch^2\nabla^2\phi) \tag{2.14}$$

Here, $\mathbf{u} = (u\ v\ w)^T$ is the velocity vector field; p the pressure scalar field; $\rho(\phi)$ and $\eta(\phi)$ are the dimensionless density and viscosity; the surface tension term will be reviewed in the next chapter (§2.2.3); Fr is the Froud number; We is the Weber number; Ch is the Cahn number and $\mathbf{g}$ is the gravitational vector.

The dimensionless shear Reynolds number, the Froud number, the Weber number, the Cahn number and the Peclet number are defined as follows:

$$Re_\tau = \frac{\tilde{\rho}\tilde{u}_\tau\tilde{h}}{\tilde{\eta}_c} = \frac{\text{inertial forces}}{\text{viscous forces}} \tag{2.15}$$

$$Fr = \frac{\tilde{u}_\tau}{\sqrt{\tilde{g}\tilde{h}}} = \frac{\text{inertial forces}}{\text{gravitational forces}} \tag{2.16}$$

$$We = \frac{\tilde{\rho}\tilde{u}_\tau^2\tilde{h}}{\tilde{\sigma}} = \frac{\text{inertial forces}}{\text{surface tension forces}} \tag{2.17}$$

$$Ch = \frac{\tilde{\epsilon}}{\tilde{h}} = \frac{\text{interfacial transition layer}}{\text{channel half height h}} \tag{2.18}$$

$$Pe_\phi = \frac{\tilde{u}_\tau\tilde{h}}{\mathcal{M}_\phi\tilde{\beta}} = \frac{\text{convection time-scale}}{\text{diffusion time-scale}} \tag{2.19}$$

Here, u_τ is the friction velocity, defined as $\tilde{u}_\tau = \sqrt{\tilde{\tau}_\omega/\tilde{\rho}}$, where $\tilde{\tau}_\omega$ is the wall shear stress and $\tilde{\rho}$ the density of the two phases; η_c is the viscosity of the phase ($\phi = -1$); $\tilde{h}$ is the channel half height; $\tilde{\epsilon}$ is the thickness of the interface and $\tilde{\sigma}$ is the surface tension; $\mathcal{M}_\phi$ is the Mobility parameter from equation (2.1) and $\tilde{\beta}$ is a positive parameter defined that describes the bulk properties. Moreover, the Cahn number Ch is determined on the basis of the computational grid. First, the grid spacing and problem size are chosen in order to properly resolve the given flow configuration, then the Ch-number is determined on the grid of the Cahn-Hillard equation (finer grid as explained in (§2.4.1)) so that there are at least four grid points across the interface and following Magaletti et al. [21], the Peclet number is always set to $Pe = 3/Ch$ in this thesis. The dimensionless density and viscosity are made non-dimensional using the phase $\phi = -1$ and are defined as follows:

$$\rho(\phi) = 1 + \frac{\lambda_\rho - 1}{2}(\phi + 1) \tag{2.20}$$

$$\eta(\phi) = 1 + \frac{\lambda_\eta - 1}{2}(\phi + 1) \tag{2.21}$$

and λ_ρ and λ_η are the respective ratios:

$$\lambda_\rho = \frac{\tilde{\rho}_{\phi=+1}}{\tilde{\rho}_{\phi=+1}} = \frac{\tilde{\rho}_+}{\tilde{\rho}_-} \tag{2.22}$$

$$\lambda_\eta = \frac{\tilde{\eta}_{\phi=+1}}{\tilde{\eta}_{\phi=+1}} = \frac{\tilde{\eta}_+}{\tilde{\eta}_-} \tag{2.23}$$

The density and viscosity are the sum of a constant part and a ϕ-dependent part. Thus, if the two phases have the same density and viscosity, their respective ϕ-dependent parts will cancel out and the Navier-Stokes equations (2.13) will simplify as follows:

$$\frac{\partial \mathbf{u}}{\partial t} + \mathbf{u} \cdot \nabla \mathbf{u} = -\nabla p + \frac{1}{Re_\tau} \nabla \cdot \left(\nabla \mathbf{u} + \nabla \mathbf{u}^T \right) + \frac{\mathbf{g}}{Fr^2} + \underbrace{\frac{3}{\sqrt{8}} \frac{Ch}{We} \nabla \cdot [\bar{\tau}_c f_\sigma(\psi)]}_{\text{Surface tension term}} \tag{2.24}$$

Surface tension term

Here, a quick summary of how to obtain the surface tension term is provided. For a more detailed overview, see [26, 30]. First, we have the following expression:

$$\frac{3}{\sqrt{8}} \frac{Ch}{We} \nabla \cdot [\bar{\tau}_c f_\sigma(\psi)], \tag{2.25}$$

where $\bar{\tau}_c$ is the dimensionless Korteweg tensor and $f_\sigma(\psi)$ is the dimensionless expression for the Equation of State (EOS). The dimensionless Korteweg tensor $\bar{\tau}_c$ can be made non-dimensional and obtained as follows:

$$\bar{\tau}_c = \frac{\tilde{\beta}/\tilde{\alpha}}{\tilde{h}^2} = |\nabla \phi|^2 \mathbf{I} - \nabla \phi \otimes \nabla \phi \tag{2.26}$$

Here, $\tilde{\alpha}$ and $\tilde{\beta}$ are positive defined parameters that describe the bulk properties and $\tilde{h}$ is the half height of the channel. And the dimensionless equation of state (EOS) $f_\sigma(\psi)$ is defined as:

$$f_\sigma(\psi) = \frac{\tilde{\sigma}(\psi)}{\tilde{\sigma}_0} \tag{2.27}$$

Here, ψ is the surfactant concentration; σ_0 is the surface tension of a clean interface and $\sigma(\psi)$ is the Langmuir EOS [18], which describes the effect of a surfactant on the interface and is defined as:

$$\tilde{\sigma}(\psi) = \tilde{\sigma}_0 (1 + \beta_s ln(1 - \psi)), \tag{2.28}$$

where β_s is the number of elasticity, a dimensionless parameter that quantifies the effect of the surfactant on the surface tension. In this thesis, a clean interface (ψ=0) is

proposed and $\sigma(\psi) = \sigma_0$, therefore:

$$f_\sigma(\psi) = \frac{\tilde{\sigma}(\psi)}{\tilde{\sigma}_0} = 1 \tag{2.29}$$

Since a clean interface ($\psi = 0$) is assumed throughout the thesis, the Cahn-Hillard equation for surfactant ψ is not covered nor used in this thesis.

2.3 Numerical method

2.3.1 Solution algorithm

The Continuity equation CE (2.12), the Navier-Stokes equations NSE (2.13) and the Cahn-Hillard equation CHE (2.14) must be rewritten in a formulation suitable for the solution algorithm. A velocity-vorticity approach is used for the flow field: The CE and NSE equations are replaced by a second-order equation for the wall-normal component of the vorticity (curl of the NSE), a fourth-order one for the wall-normal component of the velocity (another curl of the equation, so twice the curl of the NSE), the definition of the wall-normal vorticity and the CE itself. This formulation avoids the time-consuming Poisson solver for the pressure field. In the Cahn-Hillard equation a particular 'operating-splitting' technique is used. The non-linear terms $\mathbf{S}$ of the NSE and S_ϕ of the CHE are collected in their respective terms because they will be separately time-integrated using an explicit scheme and we obtain a more compact formulation overall.

Velocity-vorticity formulation

Starting with the dimensionless Navier-Stokes equations (2.13):

$$\frac{\partial \mathbf{u}}{\partial t} = \mathbf{S} + \frac{1}{Re_\tau}\nabla^2\mathbf{u} - \nabla p' \tag{2.30}$$

Here, the pressure term is divided into the mean pressure and the fluctuating component: $p = \bar{p} + p'$; The mean pressure gradient is defined as $\Pi = \nabla\bar{p}$, which will be predetermined

and drives the flow; The non-linear term $\mathbf{S}$ has been collected, as follows:

$$\begin{aligned}\mathbf{S} = &- \mathbf{u}\cdot\nabla\mathbf{u} - \frac{\lambda_\rho - 1}{2}(\phi+1)\Big(\frac{\partial\mathbf{u}}{\partial t} + \mathbf{u}\cdot\nabla\mathbf{u}\Big) - \Pi + \\ &+ \frac{1}{Re_\tau}\nabla\cdot\Big(\frac{\lambda_\eta - 1}{2}(\phi+1)(\nabla\mathbf{u} + \nabla\mathbf{u}^T)\Big) + \\ &+ \frac{\rho(\phi)\mathbf{g}}{Fr^2} + \frac{3}{\sqrt{8}}\frac{Ch}{We}\nabla\cdot\Big(|\nabla\phi|^2\mathbf{I} - \nabla\phi\otimes\nabla\phi\Big)\end{aligned} \tag{2.31}$$

To solve the system and remove the fluctuating pressure term $\nabla p'$, the curl of equation (2.30) is taken:

$$\frac{\partial\boldsymbol{\omega}}{\partial t} = \nabla\times\mathbf{S} + \frac{1}{Re_\tau}\nabla^2\boldsymbol{\omega} \tag{2.32}$$

Here, the identity $\nabla\times\nabla p' = 0$ has been used. Taking the curl again from the rewritten equation (2.32) and substituting the Continuity equation (2.12) and the identity $\nabla\times\nabla\times\mathbf{c} = \nabla(\nabla\cdot\mathbf{c}) - \nabla^2\mathbf{c}$, a fourth-order equation for the velocity field $\mathbf{u}$ is obtained:

$$\frac{\partial\nabla^2\mathbf{u}}{\partial t} = \nabla^2\mathbf{S} - \nabla(\nabla\cdot\mathbf{S}) + \frac{1}{Re_\tau}\nabla^4\mathbf{u} \tag{2.33}$$

Equations (2.32) and (2.33) are solved for the normal components of the wall vorticity ω_z and velocity w by adopting the 'velocity-vorticity' algorithm developed by [15]. Rewrite the equations for ω_z and w, respectively:

$$\frac{\partial\omega_z}{\partial t} = \frac{\partial S_y}{\partial x} - \frac{\partial S_x}{\partial y} + \frac{1}{Re_\tau}\nabla^2\omega_z \tag{2.34}$$

$$\frac{\partial(\nabla^2 w)}{\partial t} = \nabla^2 S_z - \frac{\partial}{\partial z}\Big(\frac{\partial S_x}{\partial x} + \frac{\partial S_y}{\partial y} + \frac{\partial S_z}{\partial z}\Big) + \frac{1}{Re_\tau}\nabla^4 w \tag{2.35}$$

With a suitable set of boundary conditions ω_z and w are calculated and afterwards the streamwise velocity u and the spanwise velocity v are obtained from the CE and the voritcity definition:

$$\frac{\partial w}{\partial t} = -\frac{\partial u}{\partial x} - \frac{\partial v}{\partial y} \tag{2.36}$$

$$\omega_z = \frac{\partial v}{\partial x} - \frac{\partial u}{\partial y} \tag{2.37}$$

Once the velocity field is computed, the fluctuating pressure p' can be obtained by solving a Poisson-like equation:

$$\nabla^2 p' = \nabla \cdot \mathbf{S} \tag{2.38}$$

Cahn-Hillard equation splitting

The solution of the Cahn-Hillard equation necessitate a high-order numerical scheme due to the high-order operators it involves. While reducing the stability requirements and using the same pseudo-spectral code as for the continuity and momentum equations, the equivalence can be adapted as follows:

$$\frac{\partial \phi}{\partial t} = \mathbf{S}_\phi + \frac{s}{Pe_\phi}\nabla^2\phi - \frac{Ch^2}{Pe_\phi}\nabla^4\phi \tag{2.39}$$

The operator splitting that is used is defined as follows:

$$-\frac{1}{Pe_\phi}\nabla^2\phi = +\frac{s}{Pe_\phi}\nabla^2\phi - \frac{s+1}{Pe_\phi}\nabla^2\phi, \tag{2.40}$$

where the splitting coefficient $s = \sqrt{\frac{4Pe_\phi Ch^2}{\Delta t}}$ is an anticipation here and will be calculated later in (§2.3.3) (Δt is the integration time step). The non-linear part of the Cahn-Hillard equation collects the non-linear parts and the corresponding splitting part and is defined as:

$$\mathbf{S}_\phi = -\mathbf{u}\cdot\nabla\phi + \frac{1}{Pe_\phi}\left(\nabla^2\phi^3 - (s+1)\nabla^2\phi\right) \tag{2.41}$$

2.3.2 Spectral approximation

The equations (2.34),(2.35) and (2.39) are solved using a pseudo-spectral spatial discretisation: Along the two periodic directions x and y the solutions are approximated by a Fourier transformation and for the wall-normal direction z Chebyshev polynomials are used. In order to avoid convolutions in the Fourier-Chebyshev space, the multiplication of spectral variables (i.e. convective terms) is obtained by tranforming the variable back to the physical space, taking the multiplications and then re-transforming to the Fourier-Chebyshev space. For these transformations, the Fast Fourier Transformation

FFT will be used to significantly accelerate the computation[5]. This class of algorithms is also known as a 'pseudo-spectral algorithms'. A signal f, projected along the periodic directions x and y in Fourier space, can be represented through the following sum of harmonics:

$$f(x,y,z) = \sum_{n_x=-\frac{N_x}{2}+1}^{\frac{1}{2}N_x} \sum_{n_y=-\frac{N_y}{2}+1}^{\frac{1}{2}N_y} \hat{f}(k_x,k_y,z)e^{j(k_x x+k_y y)} \tag{2.42}$$

Here, $\hat{f}$ is the Fourier coefficient of the signal in the modal coordinates (k_x, k_y) and at this point the dependence on the physical coordinate z is still given; $j = \sqrt{-1}$ is the imaginary unit of the complex representation. Both the periodic directions x and y are transformed with a Fast-Fourier Transform (FFT) imposing periodicity lengths of L_x and L_y project the velocity vector onto N_x and N_y Fourier modes in the x and y directions of the geometry of figure (2.2). For the Fast-Fourier Transformation, the variables are mapped on a uniform grid in the physical space and the nodes spacing is:

$$\Delta x = \frac{L_x}{N_x - 1} \quad \Delta y = \frac{L_y}{N_y - 1} \tag{2.43}$$

The signal is decomposed into a sum of periodic functions characterized by wavenumber and amplitude, where the wavenumber is defined as the frequency of the corresponding harmonic and the latter is the magnitude of the harmonic. Each mode n_x and n_y is defined by the following wavenumbers:

$$k_x = \frac{2\pi n_x}{L_x} \quad k_y = \frac{2\pi n_y}{L_y} \tag{2.44}$$

The Fourier basis itself is orthogonal; therefore, the Fourier transform $\hat{f}(k_x, k_y, z)$ is obtained as follows:

$$\hat{f}(k_x,k_y,z) = \frac{1}{N_x N_y} \sum_{n_x=-\frac{N_x}{2}+1}^{\frac{1}{2}N_x} \sum_{n_y=-\frac{N_y}{2}+1}^{\frac{1}{2}N_y} f(x,y,z)e^{-j(k_x x+k_y y)} \tag{2.45}$$

[5]Compare to [12], page 9

In the normal direction to the wall z the transformed signal $\hat{f}(k_x, k_y, z)$ is approximated by a sum of Chebyshev polynomials $T_n(z)$:

$$\hat{f}(k_x, k_y, z) = \sum_{n_z=0}^{N_z'} h(k_x, k_y, n_z) T_n(z) \tag{2.46}$$

Here, the prime indicates that the first term is halved and the Chebyshev polynomial order n_z in z is defined as follows:

$$T_{nz}(z) = cos[n_z cos^{-1}(z)], \tag{2.47}$$

where n_z is one of the Chebyshev modes N_z and $-1 \leq z \leq 1$ and the orthogonality holds also for the Chebyshev polynomials and the inverse transform is:

$$\hat{h}(k_x, k_y, n_z) = \frac{2}{N_z} \sum_{n_z=0}^{N_z'} \hat{f}(k_x, k_y, z) T_n(z) \tag{2.48}$$

The variables described in the Chebishev space are mapped in the physical space according to:

$$z = cos\left(\frac{n_z \pi}{N_z}\right) \tag{2.49}$$

The Chebyshev polynomials, which deliver a small grid spacing near the wall due to its distribution, allow one to resolve the large velocity gradients that occur there. For a complete review of the method, see [5]. Merging the Fourier and Chebyshev transform and adding the time dependence lead us to the following.

$$f(x, y, z, t) = \sum_{n_x=-\frac{N_x}{2}+1}^{\frac{1}{2}N_x} \sum_{n_y=-\frac{N_y}{2}+1}^{\frac{1}{2}N_y} \sum_{n_z=0}^{N_z'} \hat{f}(k_x, k_y, n_z, t) T_{n_z}(z) e^{j(k_x x + k_y y)} \tag{2.50}$$

Since the presence of products taken in the physical space, the computational algorithm needs the introduction of de-aliasing procedures also in the Chebyshev transforms, following again [5] 'the 2/3 rule' is applied, where the higher third of the modes are getting cut off and only 2/3 are considered in the pseudo-spectral multiplications.

2.3.3 Pseudo-spectral discretization of the equations

Velocity equation

Using the spectral approximation (§2.3.2) for the velocity equation (2.35) gives the following:

$$\begin{aligned}\frac{\partial}{\partial t}\Big(\frac{\partial^2}{\partial z^2}-k_{xy}^2\Big)\hat{w} &= \Big(\frac{\partial^2}{\partial z^2}-k_{xy}^2\Big)\hat{S}_z \quad - \\ &- \frac{\partial}{\partial z}\Big(ik_x\hat{S}_x+ik_y\hat{S}_y+\frac{\partial}{\partial z}\hat{S}_z\Big) \quad + \\ &+ \frac{1}{Re_\tau}\Big(\frac{\partial^2}{\partial z^2}-k_{xy}^2\Big)\Big(\frac{\partial^2}{\partial z^2}-k_{xy}^2\Big)\hat{w}\end{aligned} \tag{2.51}$$

Here, $k_{xy}^2 = k_x^2 + k_y^2$. Time discretization is done using a hybrid IMplicit EXplicit (IMEX) scheme:

i) a second-order Adams-Bashford explicit scheme is used for the non-linear terms

ii) the implicit Crank-Nicholson implicit scheme is applied to the diffusive operators

The time-discretized form of the velocity equation (2.51) reads as follows

$$\begin{aligned}&\frac{1}{\Delta t}\Big[\Big(\frac{\partial^2}{\partial z^2}-k_{xy}^2\Big)\hat{w}^{n+1}-\Big(\frac{\partial^2}{\partial z^2}-k_{xy}^2\Big)\hat{w}^{n}\Big] \quad = \\ = \;& \frac{3}{2}\Big(\frac{\partial^2}{\partial z^2}-k_{xy}^2\Big)\hat{S}_z^n-\frac{1}{2}\Big(\frac{\partial^2}{\partial z^2}-k_{xy}^2\Big)\hat{S}_z^{n-1} \quad - \\ - \;& \frac{3}{2}\frac{\partial}{\partial z}\Big(ik_x\hat{S}_x^n+ik_y\hat{S}_y^n+\frac{\partial}{\partial z}\hat{S}_z^n\Big) \quad + \\ + \;& \frac{1}{2}\frac{\partial}{\partial z}\Big(ik_x\hat{S}_x^{n-1}+ik_y\hat{S}_y^{n-1}+\frac{\partial}{\partial z}\hat{S}_z^{n-1}\Big) \quad + \\ + \;& \frac{1}{Re_\tau}\Big(\frac{\partial^2}{\partial z^2}-k_{xy}^2\Big)\Big(\frac{\partial^2}{\partial z^2}-k_{xy}^2\Big)\frac{\hat{w}^{n+1}-\hat{w}^n}{2},\end{aligned} \tag{2.52}$$

where the superscripts $n-1$, n and $n+1$ characterize the three consecutive time levels $t-\Delta t$, t and $t+\Delta t$, where Δt is the timestep. By introducing the coefficient $\gamma = \frac{\Delta t}{2Re}$,

the equation can be rewritten again:

$$\begin{aligned}
&\Big[(1-\gamma)\Big(\frac{\partial^2}{\partial z^2}-k_{xy}^2\Big)\Big]\Big(\frac{\partial^2}{\partial z^2}-k_{xy}^2\Big)\hat{w}^{n+1} \quad = \\
= \quad &\frac{3\Delta t}{2}\Big(\frac{\partial^2}{\partial z^2}-k_{xy}^2\Big)\hat{S}_z^n-\frac{\Delta t}{2}\Big(\frac{\partial^2}{\partial z^2}-k_{xy}^2\Big)\hat{S}_z^{n-1} \quad - \\
- \quad &\frac{3\Delta t}{2}\frac{\partial}{\partial z}\Big(ik_x\hat{S}_x^n+ik_y\hat{S}_y^n+\frac{\partial}{\partial z}\hat{S}_z^n\Big) \quad + \\
+ \quad &\frac{\Delta t}{2}\frac{\partial}{\partial z}\Big(ik_x\hat{S}_x^{n-1}+ik_y\hat{S}_y^{n-1}+\frac{\partial}{\partial z}\hat{S}_z^{n-1}\Big) \quad + \\
+ \quad &\Big[\gamma\frac{\partial^2}{\partial z^2}+(1-k_{xy}^2)\Big]\Big(\frac{\partial^2}{\partial z^2}-k_{xy}^2\Big)\hat{w}^n
\end{aligned} \tag{2.53}$$

The discretized form of the continuity equation (2.12) looks like this:

$$ik_x\hat{u}+ik_y\hat{v}+\frac{\partial w}{\partial z}=0 \tag{2.54}$$

Substituting the continuity equation (2.54) into the equation (2.53) and introducing the coefficient $\lambda^2=(1+\gamma k_{xy}^2)/\gamma$, one obtains the following:

$$\begin{aligned}
- \quad &\gamma\Big(\frac{\partial^2}{\partial z^2}-\lambda^2\Big)\Big(\frac{\partial^2}{\partial z^2}-k_{xy}^2\Big)^{n+1} \quad = \\
- \quad &k_{xy}^2\Big(\frac{3}{2}\hat{S}_z^n-\frac{1}{2}S_z^{n-1}\Big)\Delta t-k_{xy}^2\Big[\gamma\frac{\partial^2}{\partial z^2}+(1-\gamma k_{xy}^2)\Big]\hat{w}^n \quad - \\
- \quad &\frac{\partial}{\partial z}ik_x\Big(\frac{3}{2}\hat{S}_x^n-\frac{1}{2}S_x^{n-1}\Big)\Delta t-\frac{\partial}{\partial z}ik_x\Big[\gamma\frac{\partial^2}{\partial z^2}+(1-\gamma k_{xy}^2)\Big]\hat{u}^n \quad - \\
- \quad &\frac{\partial}{\partial z}ik_y\Big(\frac{3}{2}\hat{S}_y^n-\frac{1}{2}S_y^{n-1}\Big)\Delta t-\frac{\partial}{\partial z}ik_y\Big[\gamma\frac{\partial^2}{\partial z^2}+(1-\gamma k_{xy}^2)\Big]\hat{v}^n
\end{aligned} \tag{2.55}$$

The historical terms $\hat{H}_x^n$, $\hat{H}_y^n$, and $\hat{H}_z^n$ are defined as follows:

$$\begin{aligned}
\hat{H}_x^n &= \Big(\frac{3}{2}\hat{S}_x^n-\frac{1}{2}S_x^{n-1}\Big)\Delta t+\Big[\gamma\frac{\partial^2}{\partial z^2}+(1-\gamma k_{xy}^2)\Big]\hat{u}^n \\
\hat{H}_y^n &= \Big(\frac{3}{2}\hat{S}_y^n-\frac{1}{2}S_y^{n-1}\Big)\Delta t+\Big[\gamma\frac{\partial^2}{\partial z^2}+(1-\gamma k_{xy}^2)\Big]\hat{v}^n \\
\hat{H}_z^n &= \Big(\frac{3}{2}\hat{S}_z^n-\frac{1}{2}S_z^{n-1}\Big)\Delta t+\Big[\gamma\frac{\partial^2}{\partial z^2}+(1-\gamma k_{xy}^2)\Big]\hat{w}^n
\end{aligned} \tag{2.56}$$

Applying the historical term of equation (2.56) to equation (2.55) reads as follows:

$$\Big(\frac{\partial^2}{\partial z^2}-\lambda^2\Big)\Big(\frac{\partial^2}{\partial z^2}-k_{xy}^2\Big)\hat{w}^{n+1}=\frac{1}{\gamma}\Big[k_{xy}^2\hat{H}_z^n+\frac{\partial}{\partial z}(ik_x\hat{H}_x^n+ik_y\hat{H}_y^n)\Big] \tag{2.57}$$

The merging of all historical terms into one $\hat{H}^n = k_{xy}^2 \hat{H}_z^n + \frac{\partial}{\partial z}(ik_x \hat{H}_x^n + ik_y \hat{H}_y^n)$ yields the final equation:

$$\left(\frac{\partial^2}{\partial z^2} - \lambda^2\right)\left(\frac{\partial^2}{\partial z^2} - k_{xy}^2\right)\hat{w}^{n+1} = \frac{\hat{H}^n}{\gamma} \tag{2.58}$$

The equation for the wall-normal velocity is a fourth-order equation; thus, the Chebyshev-Tau method cannot be directly applied. It is then split into two second-order Helmholtz-like equations, so that the Chebyshev-Tau method can be applied to each of these second-order equations. Introducing an auxiliary variable $\hat{\theta} = (\frac{\partial}{\partial z^2} - k_{xy}^2)\hat{w}^{n+1}$ and the fourth-order equation is divided into two second-order ones:

$$\left(\frac{\partial^2}{\partial z^2} - \lambda^2\right)\hat{\theta} = \frac{\hat{H}^n}{\gamma} \tag{2.59}$$

$$\left(\frac{\partial^2}{\partial z^2} - k_{xy}^2\right)\hat{w}^{n+1} = \frac{\hat{\theta}}{\gamma} \tag{2.60}$$

The set of equations (2.59-2.60) can be solved with the code for different boundary conditions. For a closed-channel configuration on both sides (no-slip on both sides), the following boundary conditions will be imposed:

$$\hat{w}^{n+1}(z = \pm 1) = 0, \qquad \frac{\partial \hat{w}^{n+1}}{\partial z}(z = \pm 1) = 0 \tag{2.61}$$

For an open-channel configuration (top free-slip; bottom no-slip), the following boundary conditions will be imposed:

$$\hat{w}^{n+1}(z = -1) = 0, \qquad \frac{\partial \hat{w}^{n+1}}{\partial}(z = -1) = 0 \tag{2.62}$$

$$\hat{w}^{n+1}(z = +1) = 0, \qquad \frac{\partial^2 \hat{w}^{n+1}}{\partial z^2}(z = +1) = 0 \tag{2.63}$$

The boundary conditions are obtained from the no-slip and free-slip conditions on the wall combined with the continuity equation.

Influence matrix method:

Two separate differential equations (2.59-2.60) are obtained, but the physical boundary conditions apply only to the first problem (2.59), especially for the no-slip condition, since there are no physical boundary conditions available for the auxiliary variable $\hat{\theta}$ (For the free-slip condition, a boundary condition for $\hat{\theta}$ can be found). Thus, the

'Influence matrix method' must be used and, as an example, the method is applied to the no-slip condition:

$$\hat{\theta} = \hat{\theta}_1 + \hat{A}\theta_2 + \hat{B}\theta_3 \tag{2.64}$$

where $\hat{A}$ and $\hat{B}$ are complex constants that must be determined. The three different parts $\hat{\theta}_1$, $\hat{\theta}_2$ and $\hat{\theta}_3$ include one particular solution and two homogeneous solutions and can be obtained as follows:

$$\left(\frac{\partial^2}{\partial z^2} - \lambda^2\right)\hat{\theta}_1 = \frac{\hat{H}^n}{\gamma} \qquad \hat{\theta}_1(z=-1) = 0 \quad \hat{\theta}_1(z=+1) = 0 \tag{2.65}$$

$$\left(\frac{\partial^2}{\partial z^2} - \lambda^2\right)\theta_2 = 0 \qquad \theta_2(z=-1) = 1 \quad \theta_2(z=+1) = 0 \tag{2.66}$$

$$\left(\frac{\partial^2}{\partial z^2} - \lambda^2\right)\theta_3 = 0 \qquad \theta_3(z=-1) = 0 \quad \theta_3(z=+1) = 1 \tag{2.67}$$

Similarly, $\hat{w}^{n+1}$ is also rewritten into a particular $\hat{w}_1$ and two homogeneous solutions w_2 and w_3:

$$\hat{w} = \hat{w}_1 + \hat{A}w_2 + \hat{B}w_3 \tag{2.68}$$

Analogically to the solution of $\hat{\theta}$, the solution for $\hat{w}_1$, w_2 and w_3 is obtained applying the no-slip boundary conditions:

$$\left(\frac{\partial^2}{\partial z^2} - k_{xy}^2\right)\hat{w}_1 = \hat{\theta} \qquad \hat{w}_1(z=-1) = 0 \quad \hat{w}_1(z=+1) = 0 \tag{2.69}$$

$$\left(\frac{\partial^2}{\partial z^2} - k_{xy}^2\right)w_2 = \theta_1 \qquad w_2(z=-1) = 0 \quad w_2(z=+1) = 0 \tag{2.70}$$

$$\left(\frac{\partial^2}{\partial z^2} - k_{xy}^2\right)w_3 = \theta_2 \qquad w_3(z=-1) = 0 \quad w_3(z=+1) = 0 \tag{2.71}$$

The two unknown constants $\hat{A}$ and $\hat{B}$ can be determined in a closed channel by applying the $\frac{\partial \hat{w}^{n+1}}{\partial z} = 0$ boundary condition:

$$\frac{\partial \hat{w}_1}{\partial z}(z=-1) + \hat{A}\frac{\partial w_2}{\partial z}(z=-1) + \hat{B}\frac{\partial w_3}{\partial z}(z=-1) = 0 \tag{2.72}$$

$$\frac{\partial \hat{w}_1}{\partial z}(z=+1) + \hat{A}\frac{\partial w_2}{\partial z}(z=+1) + \hat{B}\frac{\partial w_3}{\partial z}(z=+1) = 0 \tag{2.73}$$

Or, for an open-channel configuration like this:

$$\frac{\partial \hat{w}_1}{\partial z}(z=-1) + \hat{A}\frac{\partial w_2}{\partial z}(z=-1) + \hat{B}\frac{\partial w_3}{\partial z}(z=-1) = 0 \tag{2.74}$$

$$\frac{\partial^2 \hat{w}_1}{\partial z^2}(z=+1) + \hat{A}\frac{\partial^2 w_2}{\partial z^2}(z=+1) + \hat{B}\frac{\partial^2 w_3}{\partial z^2}(z=+1) = 0 \tag{2.75}$$

$\hat{w}^{n+1}$ is obtained through the equations (2.72)-(2.75) and the solutions of equations (2.59) and (2.60) are obtained by adopting the Chebyshev-Tau solution algorithm proposed by [15]. The tridiagonal system is solved by applying the Gauss elimination procedure.

Vorticity equation

Using the spectral approximation (§2.3.2) for the vorticity equation (2.34) gives the following:

$$\frac{\partial \hat{\omega}_z}{\partial t} = ik_x\hat{S}_y - ik_y\hat{S}_x + \frac{1}{Re_\tau}\Big(\frac{\partial^2}{\partial z^2} - k_{xy}^2\Big)\hat{\omega}_z \tag{2.76}$$

Here, $k_{xy}^2 = k_x^2 + k_y^2$. The time discretization is done analogously to the velocity one, using a hybrid IMplicit EXplicit (IMEX) scheme:

i) a second-order Adams-Bashford explicit scheme is used for the non-linear terms

ii) the implicit Crank-Nicholson implicit scheme is applied to the diffusive operators

The time-discretized form of the vorticity equation (2.76) reads as follows:

$$\begin{aligned}\frac{\hat{\omega}_z^{n+1} - \hat{\omega}_z^n}{\Delta t} &= \frac{3}{2}\Big(ik_x\hat{S}_y^n - ik_y\hat{S}_x^n\Big) - \\ &- \frac{1}{2}\Big(ik_x\hat{S}_y^{n-1} - ik_y\hat{S}_x^{n-1}\Big) + \\ &+ \frac{1}{2Re}\Big(\frac{\partial^2}{\partial z^2} - k_{xy}^2\Big)(\hat{\omega}_z^{n+1} - \hat{\omega}_z^n),\end{aligned} \tag{2.77}$$

where the superscripts $n-1$, n and $n+1$ characterize the three consecutive time levels $t - \Delta t$, t and $t + \Delta t$, where Δt is the timestep. The definition of the vorticity

$\hat{\omega}_z = ik_x\hat{v} - ik_y\hat{u}$ is applied to equation (2.77):

$$\begin{aligned}\frac{\hat{\omega}_z^{n+1} - \hat{\omega}_z^n}{\Delta t} &= ik_x\Big[\Big(\frac{3}{2}\hat{S}_y^n - \frac{1}{2}\hat{S}_y^n\Big)\Delta t + \frac{1}{2Re}\Big(\frac{\partial^2}{\partial z^2} - k_{xy}^2\Big)\hat{v}^n\Big] \; - \\ &- ik_y\Big[\Big(\frac{3}{2}\hat{S}_x^n - \frac{1}{2}\hat{S}_x^n\Big)\Delta t + \frac{1}{2Re}\Big(\frac{\partial^2}{\partial z^2} - k_{xy}^2\Big)\hat{u}^n\Big] \; + \\ &+ \frac{1}{2Re}\Big(\frac{\partial^2}{\partial z^2} - k_{xy}^2\Big)\hat{\omega}_z^{n+1}\end{aligned} \tag{2.78}$$

Using the definition of $\hat{H}_x^n$, $\hat{H}_x^n$ and γ as before and collecting $\hat{\omega}_z^{n+1}$ on the left size, one obtains the following:

$$\Big(\frac{\partial^2}{\partial z^2} - \beta^2\Big)\hat{\omega}_z^{n+1} = -\frac{1}{\gamma}[ik_x\hat{H}_y^n - ik_y\hat{H}_x^n] \tag{2.79}$$

Here, β is defined as:

$$\beta^2 = \frac{1 + \gamma k_{xy}^2}{\gamma} \tag{2.80}$$

The solution for this system (2.79) is obtained again by adopting the Chebyshev-Tau method. For the closed-channel configuration, the following boundary conditions will be applied

$$\hat{\omega}^{n+1}(z = \pm 1) = 0 \tag{2.81}$$

and for the open-channel configuration (top free-slip, bottom no-slip) the boundary conditions will be defined as:

$$\hat{\omega}^{n+1}(z = -1) = 0 \qquad \frac{\partial\hat{\omega}_z^{n+1}}{\partial z}(z = +1) = 0 \tag{2.82}$$

The resulting tridiagonal equation system is again solved by the Gauss elimination technique. Once the wall-normal vorticity $\hat{\omega}_z$ and the wall-normal velocity $\hat{w}^{n+1}$ are known, the other two velocity components $\hat{u}^{n+1}$ and $\hat{v}^{n+1}$ are calculated from the spectral representation of the vorticity definition and the continuity equation:

$$-ik_y\hat{u}^{n+1} + ik_x\hat{v}^{n+1} = \hat{\omega}_z^{n+1} \tag{2.83}$$

$$-ik_x\hat{u}^{n+1} + ik_y\hat{v}^{n+1} = \frac{\partial\hat{w}^{n+1}}{\partial z} \tag{2.84}$$

Cahn-Hillard equation

The Cahn-Hillard equation (2.39) is also discretized in space by adopting the spectral representation (§2.3.2):

$$\begin{aligned}\frac{\partial\hat{\phi}}{\partial t} &= \hat{S}_\phi + \frac{s}{Pe_\phi}\Big(\frac{\partial^2}{\partial z^2} - k_{xy}^2\Big)\hat{\phi} \quad - \\ &- \frac{Ch^2}{Pe_\phi}\Big(\frac{\partial^2}{\partial z^2} - k_{xy}^2\Big)\Big(\frac{\partial^2}{\partial z^2} - k_{xy}^2\Big)\hat{\phi}\end{aligned} \tag{2.85}$$

The solution of the Cahn-Hillard equation is identified by high-frequency harmonics that need to be damped to keep the solution bounded. The usage of weakly damping schemes, such as the Crank-Nicholson used for previous equations, leads to aliased solutions[6]. For this reason, following [2] and [39], a first-order Backward-Difference Formula (BDF) is used for the first time step and an Adams-Bashforth adopted formula from the second time step on:

$$\begin{aligned}\frac{\hat{\phi}^{n+1} - \hat{\phi}^n}{\Delta t} &= \frac{3}{2}\hat{S}_\phi^n - \frac{1}{2}\hat{S}_\phi^{n-1} + \frac{s}{Pe_\phi}\Big(\frac{\partial^2}{\partial z^2} - k_{xy}^2\Big)\hat{\phi}^{n+1} \quad - \\ &- \frac{Ch^2}{Pe_\phi}\Big(\frac{\partial^2}{\partial z^2} - k_{xy}^2\Big)\Big(\frac{\partial^2}{\partial z^2} - k_{xy}^2\Big)\hat{\phi}^{n+1}\end{aligned} \tag{2.86}$$

Introducing the coefficient $\gamma_\phi = \Delta t Ch^2/Pe_\phi$ the equation (2.86) becomes:

$$\Big[\frac{1}{\gamma_\phi} - \frac{s}{Ch^2}\Big(\frac{\partial^2}{\partial z^2} - k_{xy}^2\Big) + \Big(\frac{\partial^2}{\partial z^2} - k_{xy}^2\Big)^2\Big]\hat{\phi}^{n+1} = \frac{H_\phi^n}{\gamma_\phi} \tag{2.87}$$

Here, the historical term $\hat{H}_\phi$ has been introduced:

$$\hat{H}_\phi = \hat{\phi}^n + \frac{\Delta t}{2}\Big(3\hat{S}_\phi^n - \hat{S}_\phi^{n-1}\Big) \tag{2.88}$$

One can decompose the fourth-order equations (2.87) into two equivalent second-order equations:

$$\begin{aligned}&\Big[\frac{1}{\gamma_\phi} - \frac{s}{Ch^2}\Big(\frac{\partial^2}{\partial z^2} - k_{xy}^2\Big) + \Big(\frac{\partial^2}{\partial z^2} - k_{xy}^2\Big)^2\Big) = \\ &= \Big[\Big(\frac{\partial^2}{\partial z^2} - k_{xy}^2 - \lambda_1\Big)\Big(\frac{\partial^2}{\partial z^2} - k_{xy}^2 - \lambda_2\Big)\Big]\end{aligned} \tag{2.89}$$

[6] Compare to [2], page 817 f.

Find the value of γ_1 and γ_2 by calculating the zeros of the polynomials:

$$\gamma_\phi \lambda^2 - \frac{s}{Ch^2}\gamma_\phi \lambda + 1 = 0. \tag{2.90}$$

The associated values can be obtained as follows:

$$\lambda_{1,2} = -\frac{s}{2Ch^2} \pm \frac{\sqrt{\frac{s^2}{Ch^4}\gamma_\phi^2 - 4\gamma_\phi}}{2\gamma_\phi} \tag{2.91}$$

The root square imposes some constraints on the choice of the value of s, in particular on the ability to have two real solutions:

$$\sqrt{\frac{s^2}{Ch^4}\gamma_\phi^2 - 4\gamma_\phi} \geq 0 \tag{2.92}$$

$$s \geq \sqrt{\frac{4Ch^4}{\gamma_\phi}} = \sqrt{\frac{4Pe_\phi Ch^2}{\Delta t}} \tag{2.93}$$

The choice of two coincident solutions $\lambda_1 = \lambda_2 = -s/2Ch^2 = -\sqrt{Pe_\phi Ch^2/\Delta t}$ guarantees the achievement of maximum stability and under this assumption the equation for ϕ is:

$$\left(\frac{\partial^2}{\partial z^2} - k_{xy}^2 + \frac{s}{2Ch^2}\right)^2 \hat{\phi}^{n+1} = \frac{\hat{H}_\phi}{\gamma_\phi} \tag{2.94}$$

Analogously to the vorticity and velocity equation, the auxiliary variable θ_ϕ is introduced and a further auxiliary variable $\delta = k_{xy}^2 - \frac{s}{2Ch^2}$ is defined:

$$\left(\frac{\partial^2}{\partial z^2} - \delta^2\right)\hat{\theta}_\phi = \frac{\hat{H}_\phi}{\gamma_\phi} \tag{2.95}$$

$$\left(\frac{\partial^2}{\partial z^2} - \delta^2\right)\hat{\phi}^{n+1} = \hat{\theta}_\phi \tag{2.96}$$

These equations are solved by imposing the following boundary conditions, where the first one accounts for a normal contact angle on the interface at the walls and the latter one for a no-flux condition of chemical potential through the walls:

$$\frac{\partial \hat{\phi}^{n+1}}{\partial z}(z = \pm 1) = 0 \qquad \frac{\partial^3 \hat{\phi}^{n+1}}{\partial z^3}(z = \pm 1) = 0 \tag{2.97}$$

The boundary conditions on $\hat{\theta}_\phi$ are in the first and third derivatives, so there is no need to apply the influence matrix method, since:

$$\frac{\partial}{\partial z}\Big(\frac{\partial^2}{\partial z^2} - \delta^2\Big)\hat{\phi}^{n+1} = \frac{\partial^3 \hat{\phi}^{n+1}}{\partial z^3} = \frac{\partial \hat{\theta}_\phi^{n+1}}{\partial z} \tag{2.98}$$

As a consequence, equation (2.95) is solved using this boundary condition

$$\frac{\partial \hat{\theta}_\phi^{n+1}}{\partial z}(\pm 1) = 0 \tag{2.99}$$

and equation (2.96) is solved as follows:

$$\frac{\partial \hat{\phi}}{\partial z}(\pm 1) = 0 \tag{2.100}$$

This solution is again obtained by applying the adopted Chebyshev-Tau method [15] to equations (2.95-2.96) and solving the resulting tridiagonal system via a Gauss elimination procedure.

2.4 Code implementation

The pseudo-spectral algorithm presented in (§2.3) for the solution of the set of equations (2.12-2.14) in section (§2.2.3) has been implemented in an in-house parallel FORTRAN 90 code. The parallelization is based on a 2D decomposition (pencil decomposition) and a MPI (Message Passing Interface) approach is adopted. Therefore, the workload can be divided among independent MPI tasks and the computational domain is uniformly distributed among all the tasks. Each task can work independently of each other, expect the communication between the tasks. The distribution of the computational domain is defined with two parameters, $N_{y,CPU}$ & $N_{z,CPU}$, and these parameters define their partitioning of the domain along the y- and z-directions. Each task holds all points in the x-direction in physical space and a fraction of the points in the y- and z-direction. A Fourier transform along the x-direction can be easily taken and the Fourier or Chebyshev transforms need all the points along the transforming direction, respectively. Once the transform in the x-direction is done, the pencils are transposed and the data are communicated with the aid of the MPI communicator

among the miscellaneous tasks. Afterward, each task holds all the points along the y-direction and only a fraction in the remaining directions. Then, the Fourier transforms in the y-direction are taken. Then again, the pencils are transposed and the Chebyshev transform in the z-directions are taken. In the modal space, the computational domain is divided along the x- and y-directions and each task holds all the points in the direction normal to the wall. The entire process is shown in figure (2.3):

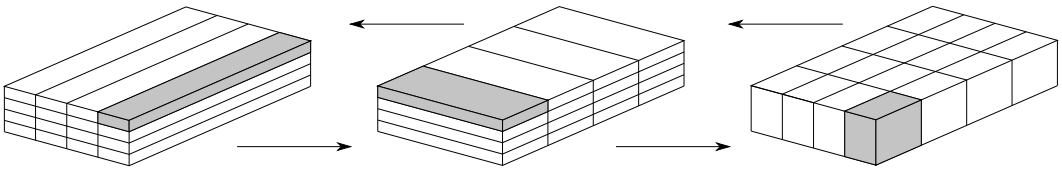

Figure 2.3 – Transforms between the physical and the modal space and vice versa (Left: Pencil decompositon in physical space; Right: Pencil decomposition in modal space) [26]

To summarize the process (2.3) from physical to modal space:

i. 1D Fourier transformation along the x-direction

ii. Pencil transposition

iii. 1D Fourier transformation along the y-direction

iv. Pencil transposition

v. 1D Chebyshev transformation along the z-direction

The transform from modal to physical space follows the same path backward.

Code structure

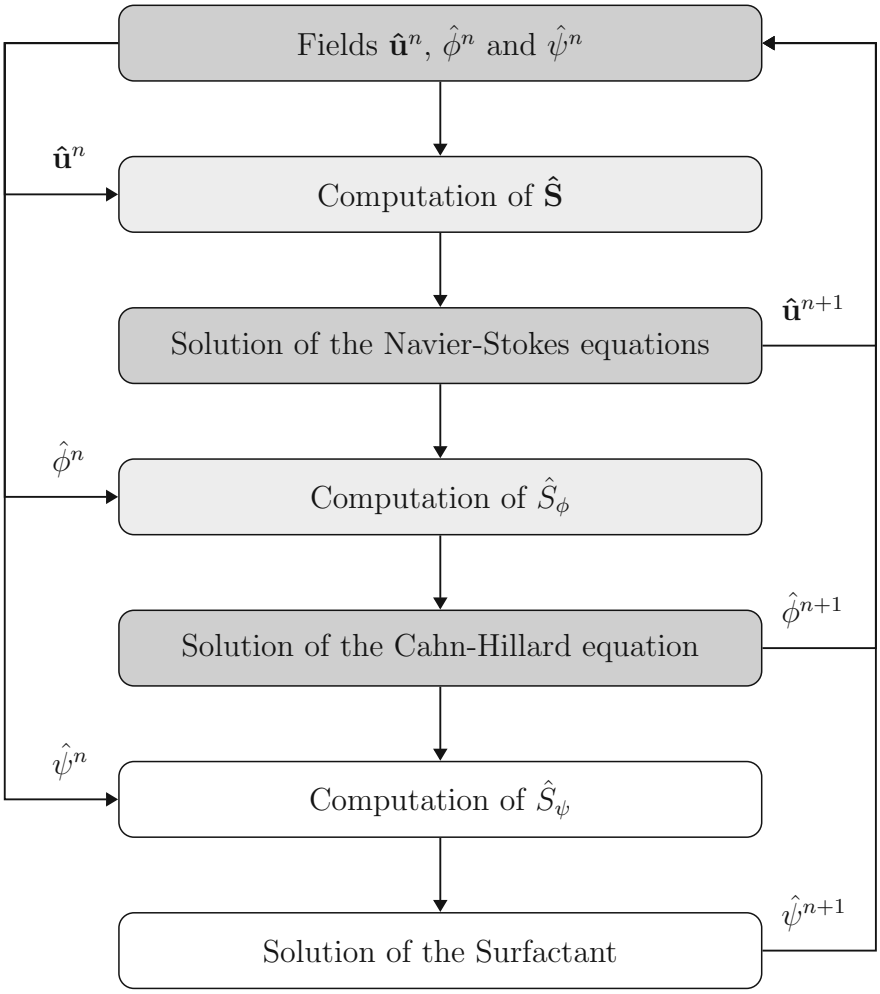

Figure 2.4 – Scheme for the numerical solver

Here, an overview of the scheme that is implemented in the code is given and can be seen in figure (2.4). Starting with the initial fields $\hat{\mathbf{u}}^n$, $\hat{\phi}^n$ and $\hat{\psi}^n$ at each time step n, for each equation the respective non-linear terms $\hat{\mathbf{S}}$, $\hat{S}_\phi$ and $\hat{S}_\psi$ are computed in the physical space and then re-transformed in the spectral space[7]. After this operation is completed, the unknown of the equation in the timestep $n+1$ is obtained using the implemented Helmholtz solver (Helmholtz-like equations). For the sake of completeness, the computation of the surfactant ψ is also shown in the figure (2.4) but will not be further discussed in this thesis, expect of the next chapter, because a clean interface (ψ=0) is assumed in this thesis (§2.2.3).

[7] Convolutions are avoided, refer back to chapter (§2.3.2)

2.4.1 Implementation of the multiple-grid approach

Before the implementation of the multiple-grid Phase Field Method approach is explained in detail, an overview of the current status is given. The present in-house code is written on the coarse grid for the Continuity equation CE (2.12,2.101), the Navier-Stokes equations NSE (2.13,2.102) and the Cahn-Hillard equation CHE (2.14,2.103). However, the Cahn-Hillard-like equation for the surfactant ψ (2.104) is already implemented on the fine grid. The aim of this work is to extend the code so that the Cahn-Hillard equation for the phase-field ϕ is also available on the fine grid. First, a small recap of the set of equations is given, where also the Cahn-Hillard-like equation for the surfactant ψ (2.104) is mentioned to give a more complete overview of the internal code:

$$\nabla \cdot \mathbf{u} = 0 \tag{2.101}$$

$$\rho(\phi)\frac{\partial \mathbf{u}}{\partial t} + \rho(\phi)\Big(\mathbf{u}\cdot\nabla\mathbf{u}\Big) = -\nabla p + \frac{1}{Re_\tau}\nabla\cdot\Big(\eta(\phi)(\nabla\mathbf{u}+\nabla\mathbf{u}^T)\Big) + \frac{\rho(\phi)\mathbf{g}}{Fr^2} + \underbrace{\frac{3}{\sqrt{8}}\frac{Ch}{We}\nabla\cdot[\bar{\tau}_c f_\sigma(\psi)]}_{\text{Surface tension term}} \tag{2.102}$$

$$\frac{\partial \phi}{\partial t} + \mathbf{u}\cdot\nabla\phi = \frac{1}{Pe_\phi}\nabla^2(\phi^3 - \phi - Ch^2\nabla^2\phi) \tag{2.103}$$

$$\frac{\partial \psi}{\partial t} + \mathbf{u}\cdot\nabla\psi = \frac{Pi}{Pe_\psi}\nabla^2\psi + \frac{1}{Pe_\psi}\nabla\cdot\Big(\psi(1-\psi)\nabla C_{\psi\phi}\Big) \tag{2.104}$$

The different parameters for the CE (2.101), the NSE (2.102) and the CHE (2.103) are already explained in detail in section (§2.2.3). For completeness, the parameters for the surfactant equation (2.104) are defined as follows:

$$Pi = \frac{\tilde{\lambda}_\psi}{\tilde{\beta}^2} \quad Pe_\psi = \frac{\tilde{\alpha}\tilde{u}_\tau\tilde{h}}{\tilde{\beta}_\psi^2} \quad C_{\psi\phi} = -\frac{1}{2}(1-\psi^2)^2 + \frac{\psi^2}{2E_x} \quad E_x = \frac{\tilde{\beta}}{\tilde{s}_\psi} \tag{2.105}$$

Here, the Peclet number of the surfactant Pe_ψ, is the ratio of convective and diffusive phenomena; Pi is a dimensionless factor, which controls the adsorption dynamics of the surfactant from the bulk to the interface and vice versa; the parameter E_x controls the solubility of the surfactant in the bulk of the two phases. For example, high values of E_x allow a high concentration of the surfactant in the bulk.

How is the finer grid for the phase-field ϕ achieved?

A review on how exactly the multiple-grid is implemented, compared to the present code, is shown here. The scheme of the numerical code can be obtained in figure (2.4):

i) Velocities $\hat{\mathbf{u}}$ are initialized on the coarse grid;
Phase field $\hat{\phi}$ is initialized on the fine grid;
Surfactant $\hat{\psi}$ is initialised on the fine grid

ii) The *surface tension term* is calculated on the fine grid and then transformed onto the coarse grid and added to the collection of non-linear terms $\hat{\mathbf{S}}$

iii) Helmholtz-equation for the Navier-Stokes equations are solved on the coarse grid

iv) Velocities $\hat{\mathbf{u}}$ are transformed onto the fine grid and the non-linear term of the Cahn-Hillard equation $\hat{S}_\phi$ is calculated

v) Helmholtz-equation for the Cahn-Hillard equation is solved on the fine grid

vi) Non-linear term of the Cahn-Hillard equation $\hat{S}_\psi$ is calculated

vii) Helmholtz-equation for the Cahn-Hillard-like surfactant equation is solved on the fine grid

Pictorial representation

A pictorial representation of the implementation of the multiple-grid approach can be seen in figure (2.5).

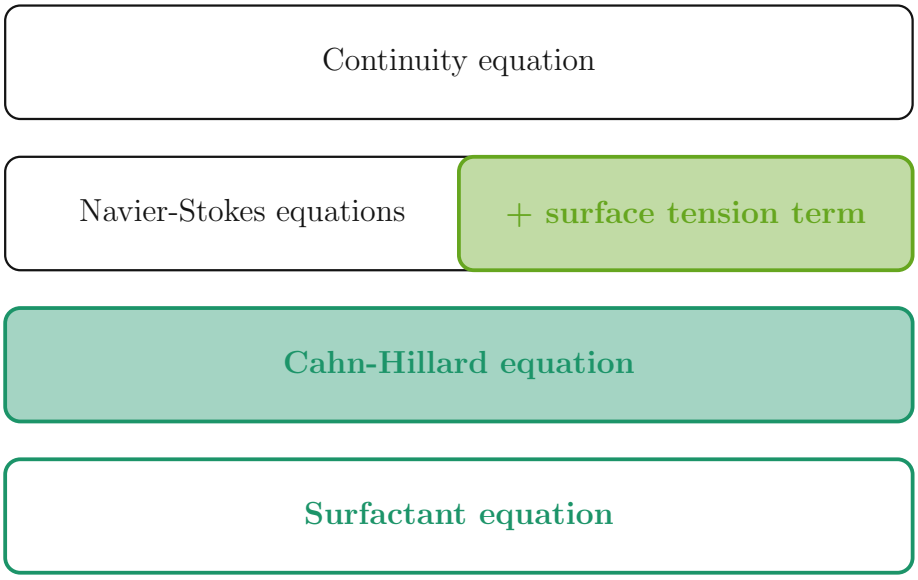

Figure 2.5 – Implementation of the multiple-grid approach - A color-filled box means that the code has changed for the multiple-grid approach - Black frame → coarse grid; Lime green frame → calculated on fine grid, then transformed to the coarse grid; Dark green frame → fine grid

3

Validation & Results

In this chapter, the implementation of the multiple-grid has been validated. Therefore, two benchmarks are used and compared with the current internal code and with suitable analytical or numerical solutions. The first benchmark evaluates the deformation of a droplet in a shear flow. For the second, a thin sheet layer is placed in the center of a 3D turbulent channel flow.

3.1 Droplet in a shear flow - 2D Benchmark

First, the implemented multiple-grid approach is benchmarked in a single droplet set-up. Therefore, a circular droplet is placed in the middle of two walls that move with constant velocity in the opposite direction under the circumstance of a laminar flow (Fig. (3.1)). The induced shear flow deforms the droplet and in the beginning there is an initial transient until a steady-state shape and the corresponding angle are reached. The shape itself is determined by a competition between viscous forces that try to elongate the droplet and surface tension forces that try to keep the initial shape. This competition is represented by the dimensionless parameter 'Capillary number' Ca and the viscosity ratio λ_η, which was already introduced in equation (2.23):

$$Ca = \frac{We}{Re_\tau}\frac{\tilde{d}}{2\tilde{h}} = \frac{\tilde{u}_w\tilde{\eta}_c\tilde{d}}{\tilde{\sigma}2\tilde{h}} \qquad \lambda_\eta = \frac{\tilde{\eta}_d}{\tilde{\eta}_c} \tag{3.1}$$

The Capillary number Ca describes the ratio of viscous forces to surface tension forces. The viscosity ratio λ_η is the relationship between the viscosity of the droplet $\tilde{\eta}_d$ and the viscosity of the external fluid $\tilde{\eta}_c$. The velocity $\tilde{u}_w$ is the wall velocity; $\tilde{d}/2\tilde{h}$ is a scaling factor because previous works used the droplet radius $\tilde{d}/4$ as a length scale instead of $\tilde{h}$,

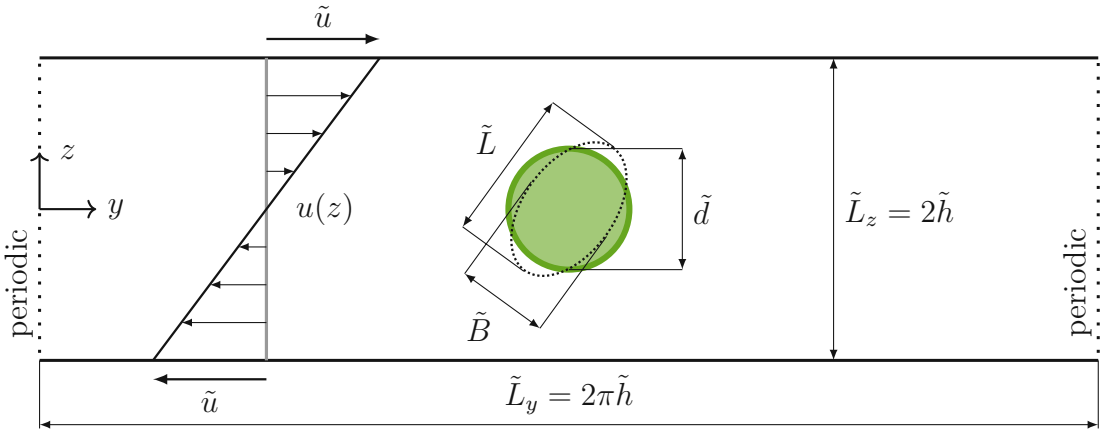

Figure 3.1 – A single droplet of diameter $\tilde{d} = 0.8\tilde{h}$ in a shear flow. The green circle shows the initial shape of the droplet and the dotted line indicates the final steady state shape (L ... major axis (length); B ... minor axis (breath)). The velocity profile $u(z)$ is also shown and is responsible for the droplet deformation. A periodic boundary condition is applied on the left and on the right side.

which is used in the internal code. The deformation parameter D is defined as follows:

$$D = \frac{\tilde{L} - \tilde{B}}{\tilde{L} + \tilde{B}} \tag{3.2}$$

Here, L is the major axis (=length) and B is the minor axis (=breath) of the circular droplet, as shown in the figure (3.1). One of the reasons why this benchmark is so popular is that in addition to endless numerical [13, 16] and experimental [25] results, there is also an analytical solution for it. This analytical solution was found by Taylor [34, 35] and describes the deformation of a small circular droplet as a function of the Capillary number Ca. This solution was corrected later by Shapira and Haber [29], which also accounts for the effect of lateral confinement on the droplet deformation. The correction of these two also includes a factor that considers the scaling factor $\tilde{d}/4\tilde{h}$:

$$D = \frac{16 + 19\lambda_\eta}{16 + 16\lambda_\eta} Ca \left[1 + C_{SH} \frac{3.5}{2} \left(\frac{\tilde{d}}{4\tilde{h}}\right)^3\right] \tag{3.3}$$

Here, C_{SH} is a numerical coefficient equal to 5.6996 [29]. This equation holds for $D < 0.3$. For a small Capillary number Ca (high surface tension), the droplet wants to remain in a quasicircular shape; on the contrary, if the Capillary number Ca is high enough, then the droplet can undergo a breakage.

Angle $\hat{\theta}_{th}$ is measured, when the deformed droplet reaches steady state, from the x-axis to the major axis of the ellipsoid and is obtained as follows [27]:

$$\hat{\theta}_{th} = \frac{\pi}{4} - \frac{(19\lambda_\eta + 16)(2\lambda_\eta + 3)}{80(1 + \lambda_\eta)} \cdot Ca \tag{3.4}$$

In the end, a time and memory comparison is made, where different code setups are compared against each other once on the in-house computer and once on the supercomputer Marconi-100.

3.1.1 Problem definiton

A ciruclar droplet with diameter $\tilde{d} = 0.8\tilde{h}$, is placed in the center of the channel, as shown in figure (3.1). The two walls move in an opposite direction with constant velocity $u(z) = \pm 1$ along the x-direction ($v(z)$ and $w(z) = 0$). The Reynolds number is set to $Re_\tau = 0.1$ to ensure creeping flow conditions (negligible inertia). The two-dimensional computational domain is set to $L_y = 2\pi h$ and $L_z = 2h$ in the y- and z-direction and has been discretized with $N_y \times N_z = 512 \times 513$ grid points in the streamwise and wall-normal direction. The Cahn number is set to $Ch = 0.02$, which leads to a Peclet number $Pe_\phi = 3/Ch = 150$, see section (§2.2.3) or Magaletti et al. [21]. Moreover, the value of the Cahn number, $Ch = 0.02$, satisfies the requirements for an accurate description of the phase-field and its steep gradients across the interface. The density ratio is set to $\lambda_\rho = 1$. Parameters $Re_\tau = 0.1$, $Ch = 0.02$ and $Pe_\phi = 150$ are kept fixed during all simulations considered. Two different viscosity ratios are used in the benchmark:

- $\boldsymbol{\lambda_\eta = 1}$ → Checks if the matched density and viscosity case (equation (2.24)) matches the current version of the in-house code and compares it in addition to the analytical solution obtained by Shapira and Haber [29].
- $\boldsymbol{\lambda_\eta = 0.1}$ → Checks the non-matched viscosity case with the same benchmarks used.

For both viscosity ratios, different values of the Capillary number Ca were selected and set using the Weber number We in the in-house code ($We = 2.5 \cdot Re_\tau \cdot Ca$):

- $Ca = 0.0625 \quad \rightarrow \quad We = 0.015625$
- $Ca = 0.1250 \quad \rightarrow \quad We = 0.03125$
- $Ca = 0.1875 \quad \rightarrow \quad We = 0.046875$

3.1.2 Results

The table below shows three different simulations that were performed for each viscosity ratio and the corresponding Capillary numbers Ca and will be compared later with the analytical solution.

Code	exp	Grid NSE	Grid CHE	Re	Ch	Pe_ϕ	Δt
BC	-	512x513	512x513	0.1	0.02	150	2.5e-5
ME1	1x1	512x513	512x513	0.1	0.02	150	2.5e-5
ME2	2x2	256x257	512x513	0.1	0.02	150	2.5e-5

Table 3.1 – Overview of the simulations for the 2D droplet;
BC ... base code;
MEx ... developed code with expansion factor

Viscosity ratio $\lambda_\eta = 1.0$

The analytical solution for the deformation D and steady-state angle θ_{th} at the viscosity ratio $\lambda_\eta = 1.0$ is obtained as follows for the different Capillary numbers Ca:

$$D = \frac{16 + 19\lambda_\eta}{16 + 16\lambda_\eta} Ca \left[1 + C_{SH} \frac{3.5}{2} \left(\frac{\tilde{d}}{4\tilde{h}}\right)^3\right] = 1.181 \cdot Ca \tag{3.5}$$

$$\hat{\theta}_{th} = \frac{\pi}{4} - \frac{(19\lambda_\eta + 16)(2\lambda_\eta + 3)}{80(1 + \lambda_\eta)} \cdot Ca = \frac{\pi}{4} - \frac{35}{32} \cdot Ca \tag{3.6}$$

In this comparison, the two parameters are plotted over t^+ (inner time scale), whereby $t^+ = \Delta t \cdot timesteps \cdot Re_\tau$ (Δt ... integration timestep). It could be shown, in the figures (3.2-3.5), that between the current in-house code (BC) and the code developed with the expansion factor = 1 (ME1) there is no difference, for both the deformation D and the steady-state angel $\hat{\theta}_{th}$, and they are equivalent for the matched viscosity / density case. Furthermore, no significant differences were found between the current internal code (BC) and the expanded code developed (ME2). These tests not only revealed a good match between themselves, but also did not reveal significant differences between the codes (BC, ME1 and ME2) and the analytical solution, which is shown in figure (3.5). Besides that, it can be observed that with increasing Capillary number Ca, the time to convergence to the analytical solution also increases, for both the deformation D and the steady-state angel $\hat{\theta}_{th}$.

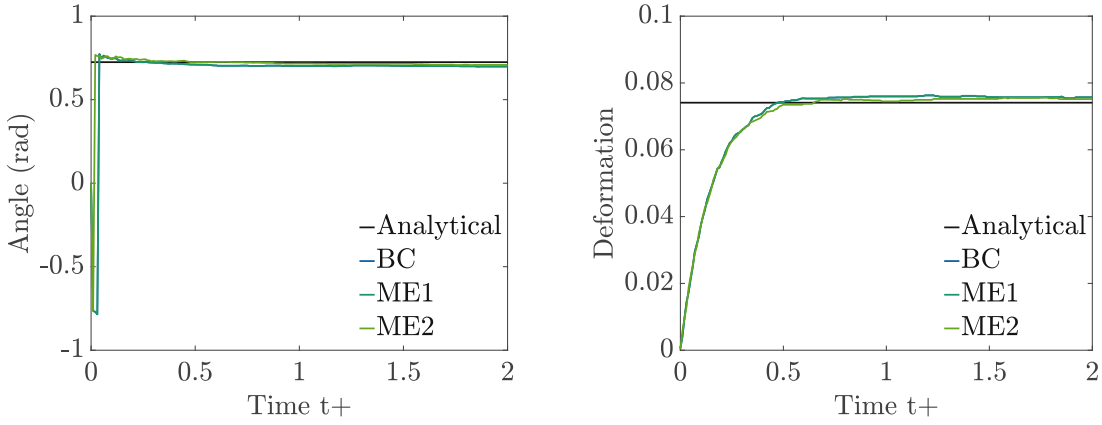

(a) Angle (b) Deformation

Figure 3.2 – $\lambda_\eta = 1$ - Capillary number Ca=0.0625

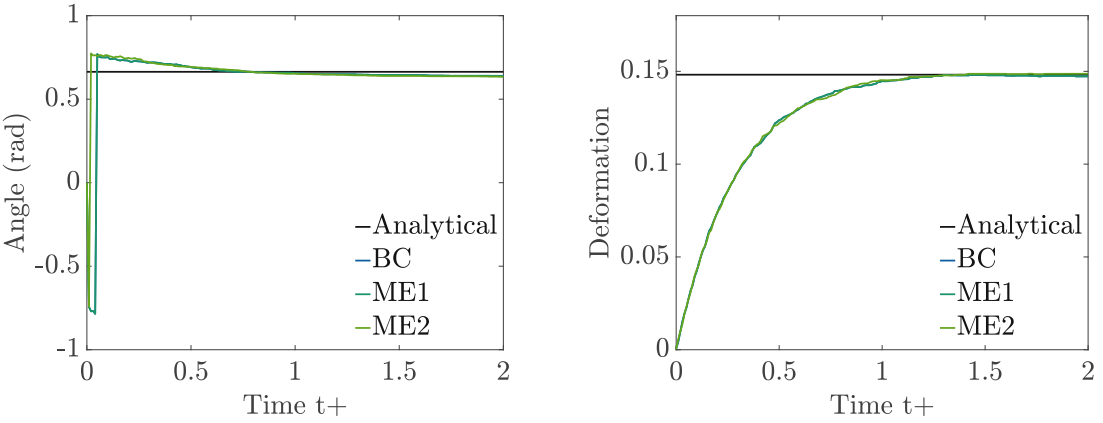

(a) Angle (b) Deformation

Figure 3.3 – $\lambda_\eta = 1$ - Capillary number Ca=0.125

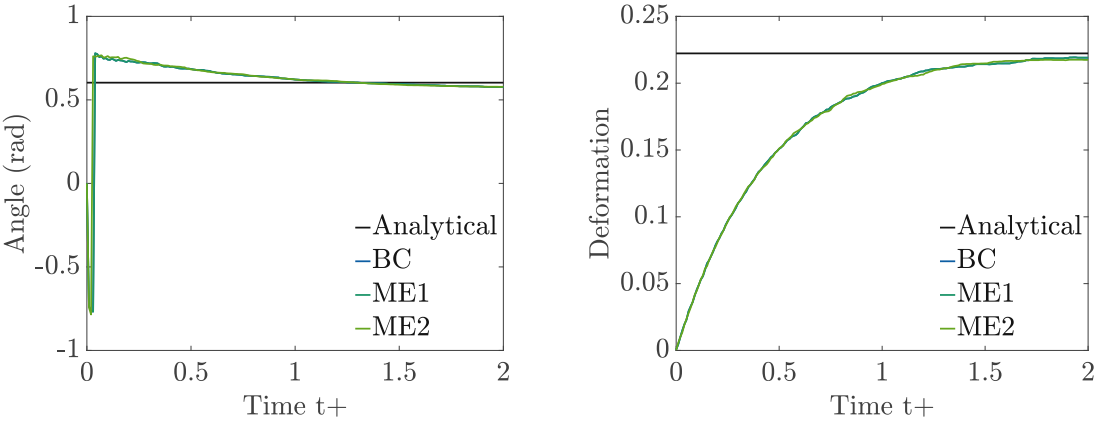

(a) Angle (b) Deformation

Figure 3.4 – $\lambda_\eta = 1$ - Capillary number Ca=0.1875

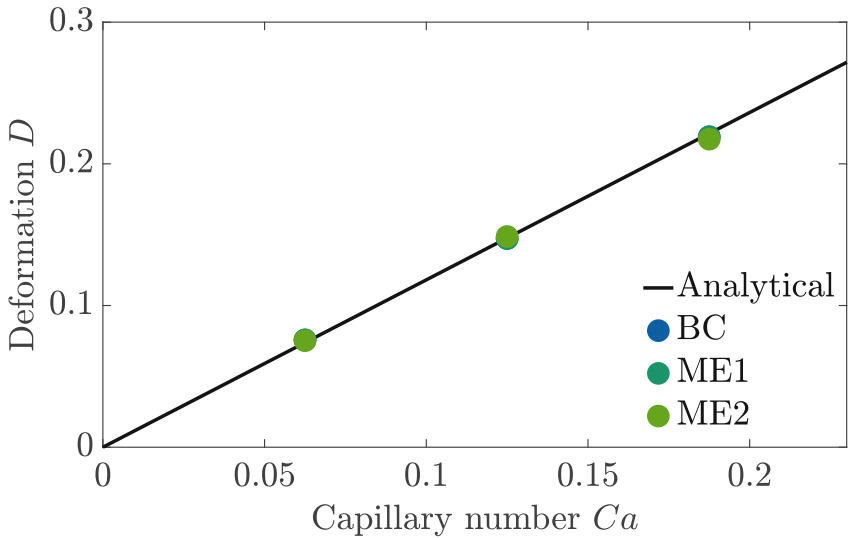

Figure 3.5 – Summary of the comparison - $\lambda_\eta = 1$ - Different Capillary numbers and their respective deformations are compared with the analytical solution from Shapira et al. (based on Taylor) [29]

Viscosity ratio $\lambda_\eta = 0.1$

The analytical solution for the deformation D and steady-state angle θ_{th} at the viscosity ratio $\lambda_\eta = 0.1$ is obtained as follows for the different Capillary numbers Ca:

$$D = \frac{16 + 19\lambda_\eta}{16 + 16\lambda_\eta} Ca \left[1 + C_{SH} \frac{3.5}{2} \left(\frac{\tilde{d}}{4\tilde{h}}\right)^3\right] = 1.0982 \cdot Ca \tag{3.7}$$

$$\hat{\theta}_{th} = \frac{\pi}{4} - \frac{(19\lambda_\eta + 16)(2\lambda_\eta + 3)}{80(1 + \lambda_\eta)} \cdot Ca = \frac{\pi}{4} - \frac{179}{275} \cdot Ca \tag{3.8}$$

Again, it could be shown that the current internal code (BC) and the new code developed with expansion factor=1 (ME1) are equivalent and there are no visible or data-driven differences, as seen in the figures (3.6-3.9). The angle and deformation of the viscosity ratio $\lambda_\eta = 0.1$ with the expanded new code (ME2) are even closer to the solution of the two previously mentioned ones (BC and ME1). The effects of the Capillary number Ca on the convergence are similar to the results mentioned above for the viscosity ratio $\lambda_\eta = 1.0$. With increasing Capillary number Ca, the time of convergence also increases. The analysis also shows that with an increase in Capillary number Ca, all three simulations (BC, ME1 and ME2) tend to overshot the analytical solution slightly more, which is summarized in figure (3.9).

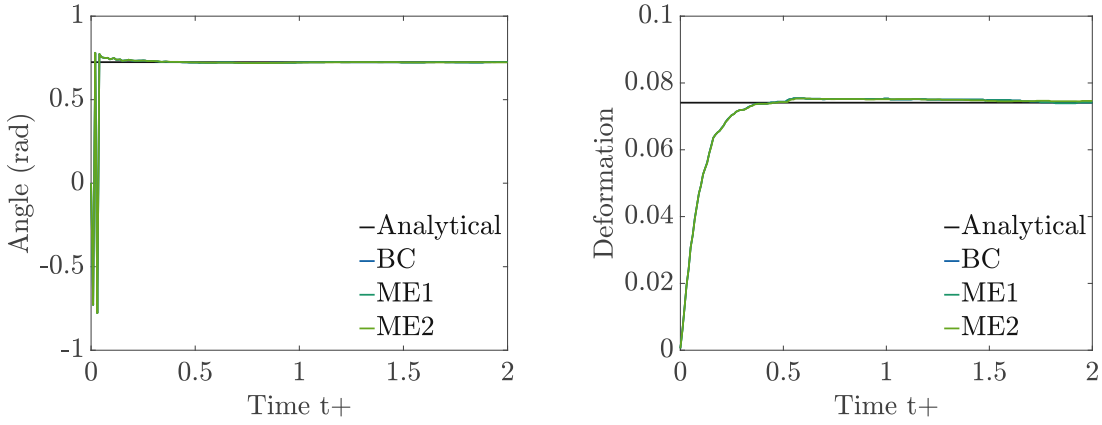

(a) Angle (b) Deformation

Figure 3.6 – $\lambda_\eta = 0.1$ - Capillary number Ca=0.0625

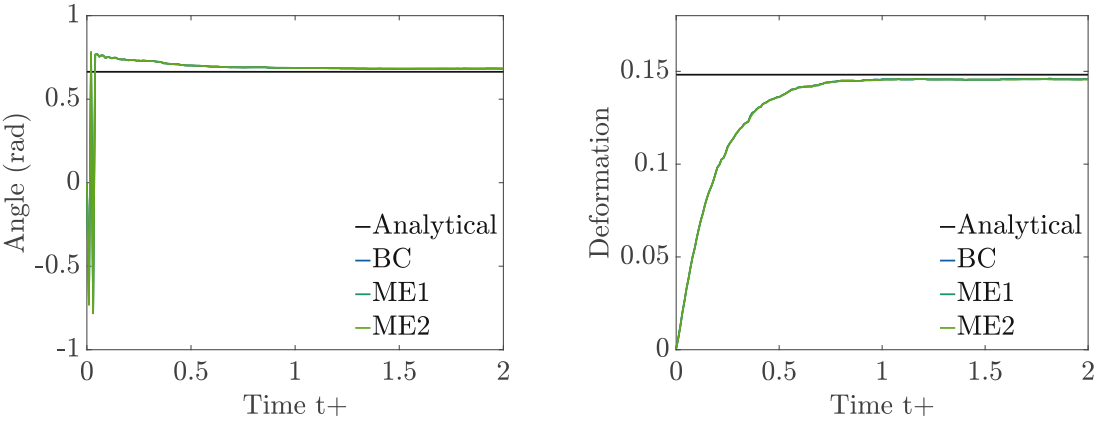

(a) Angle (b) Deformation

Figure 3.7 – $\lambda_\eta = 0.1$ - Capillary number Ca=0.125

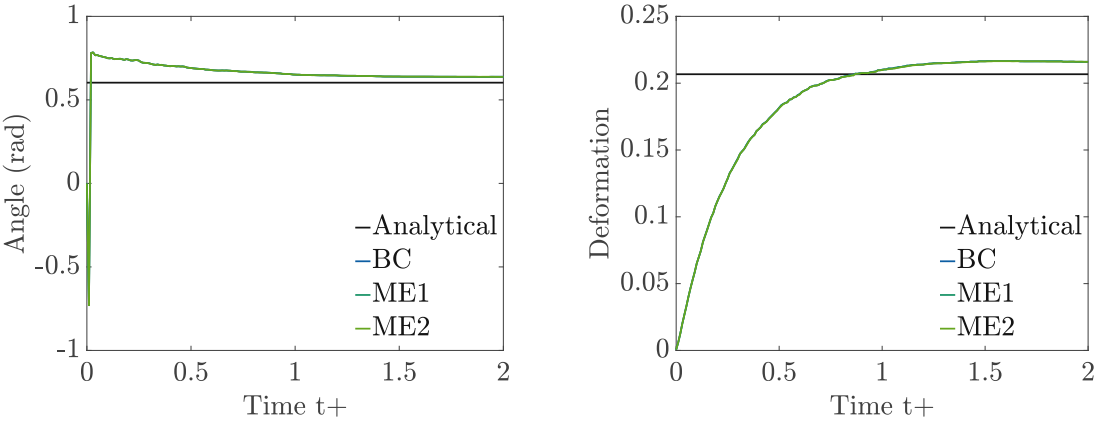

(a) Angle (b) Deformation

Figure 3.8 – $\lambda_\eta = 0.1$ - Capillary number Ca=0.1875

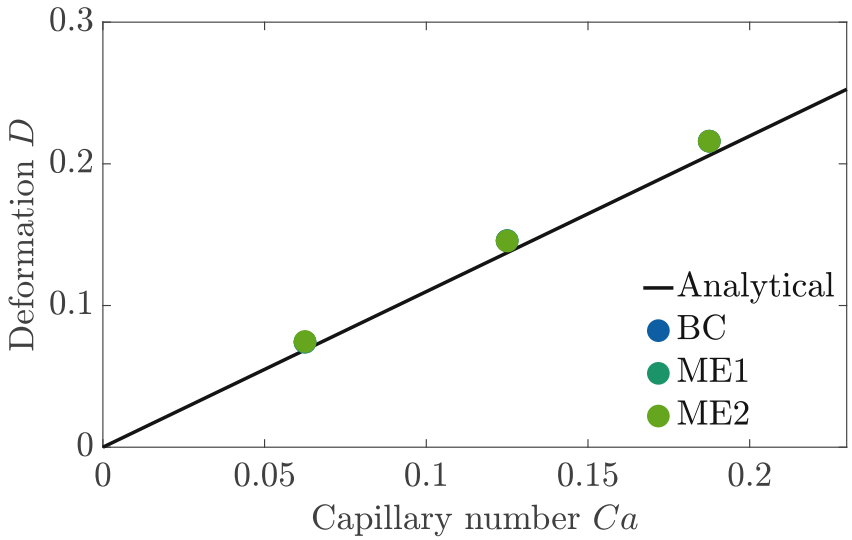

Figure 3.9 – Summary of the comparison - $\lambda_\eta = 0.1$ - Different Capillary numbers and their respective deformations are compared with the analytical solution from Shapira et al. (based on Taylor) [29]

Time and memory comparison - S21

Code	exp	Grid NSE	Grid CHE	Re	Ch	Pe_ϕ	λ_η	Ca
BC	-	512x513	512x513	0.1	0.02	150	1	0.1875
BC	-	1024x1025	1024x1025	0.1	0.01	300	1	0.1875
ME1	1x1	512x513	512x513	0.1	0.02	150	1	0.1875
ME2	2x2	512x513	1024x1025	0.1	0.01	300	1	0.1875

Table 3.2 – Overview of the simulations for the 2D droplet (NYCPU=1, NZCPU=64);
BC ... base code;
MEx ... developed code with expansion factor x;

Due to the circumstance that a 2D simulation was performed, NYCPU=1, where NYCPU accounts for the number of divisions in the domain for parallelization (y-direction in the physical space, z-direction in the modal space) and NZCPU $=2^6 = 64$ (NZCPU ... number of divisions of the domain for parallelization (z-direction when in physical space, y-direction when in modal space) where selected. No significant differences were found between the current code, the new code developed and the analytical solution in the results section before. Thus, an investigation on how much time, RAM (random-access memory - important during the simulation) and hard disk

storage (important after the simulation) can be saved was obtained. This investigation was first conducted on the internal server of our institute, called S21, where it was also possible to observe the RAM used during the simulation and compare them with each other. A random-access memory (RAM), also called working memory, is needed during simulations and specifies how much workload the computer/server is capable of. A summary of the simulations used for these benchmarks can be obtained from the table (3.2). In figure (3.10), it can be seen that the same RAM is needed for the simulation for (BC-512x513) and (ME1-512x513) and, furthermore, that we can save up to almost 30% in RAM if the newly developed expanded code (ME2-1024x1025) is used instead of the current code on a fine grid (BC-1024x1025). Moreover, the expanded version (ME2-1024x1025) needs 1.5 times more RAM than the non-expanded code (ME1-512x513), but be aware that also a better resolution of the phase-field is achieved. The same results can also be extended to the hard disk space.

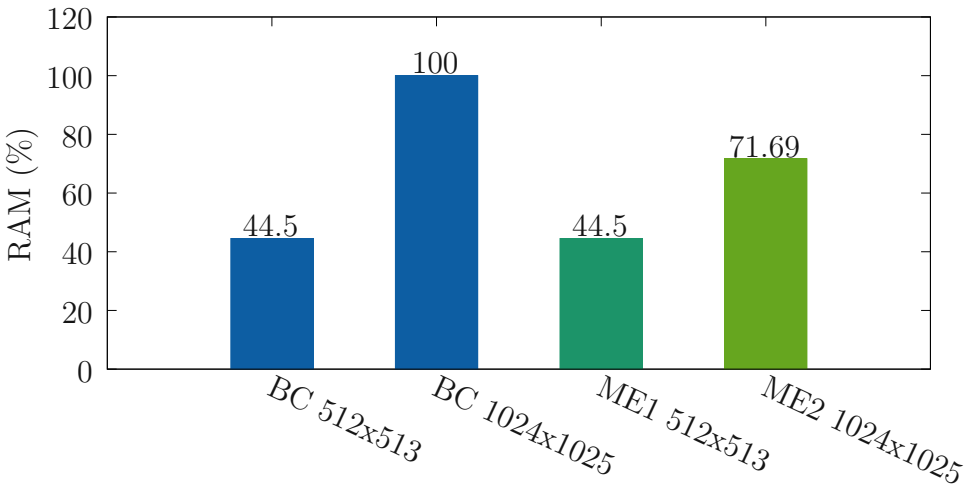

Figure 3.10 – Memory comparison - S21 (NYCPU=1, NZCPU=64)

For the time comparison (figure (3.11)), the corresponding timesteps are always obtained in the same way. There were five simulations for each of the results listed in the tab. (3.2) or also shown in fig.(3.11). And after 1000 timesteps, first an estimate of the average value for each simulation was taken for one timestep and afterwards the five different values were averaged again to obtain an overview for the time used for a timestep for the different configurations. Therefore, similar evaluations can be obtained for the

time-difference between (BC-512x513) and (ME1-512x513). Furthermore, the savings of up to 30% between the new devloped code (ME2-1024x1025), which only expands the Cahn-Hillard equation (2.14), and the internal code (BC-1024x1025), where the Navier-Stokes equations (2.13) were also expanded, is also similar to the previous observation. Compared to the memory comparison (3.10), the jump from the coarse grid (BC-512x513, ME1-512x513) to the fine grid (BC-1024x1025), (ME2-1024x1025) is significantly bigger.

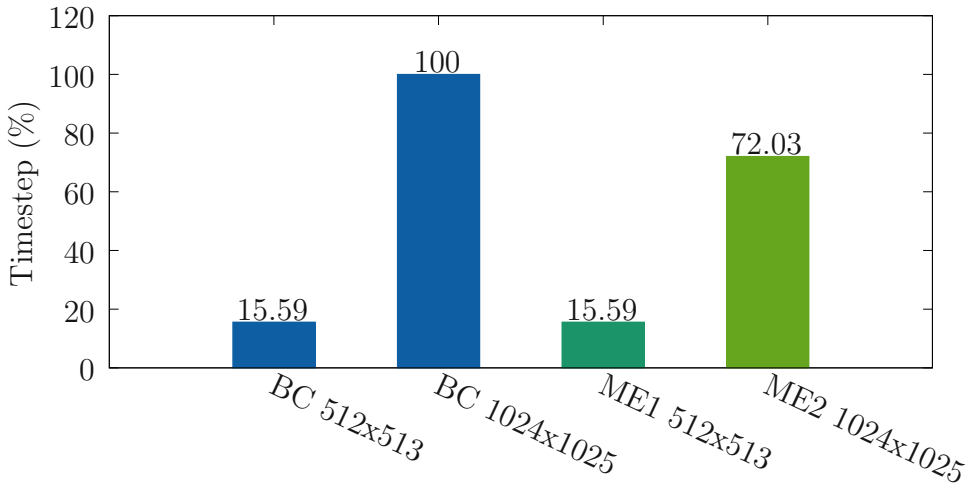

Figure 3.11 – Time comparison - S21 (NYCPU=1, NZCPU=64)

Time - Marconi 100

After promising results of the time and memory comparison on the institute's internal server, a time comparison on a supercomputer was completed. Therefore, the 'Marconi 100' has been provided to me by my supervisors for these simulations. Here is a short summary of its specifications:

- Nodes: 980
- Processors: 2x16 cores IBM POWER9 AC922 at 3.1 GHz
- Accelerators: 4 x NVIDIA Volta V100 GPUs, Nvlink 2.0, 16GB
- Cores: 32 cores/node
- RAM: 256 GB/node
- Peak Performance: 32 PFlop/s

Again, since a 2D simulation was performed, NYCPU=1, where NYCPU accounts for the number of divisions in the domain for parallelization (y-direction in physical space, z-direction in modal space) abd NZCPU $=2^6 = 64$ (NZCPU ... number of divisions of the domain for parallelization (z-direction when in physical space, y-direction when in modal space) where selected. The times per timestep are obtained in the same way as for the S21-comparison and the results are also likewise. The new developed code (ME2-512x513), which expands the phase variable on a fine grid, performs similarly well and thus is portable across different machines. The complete results can be seen in figure (3.12):

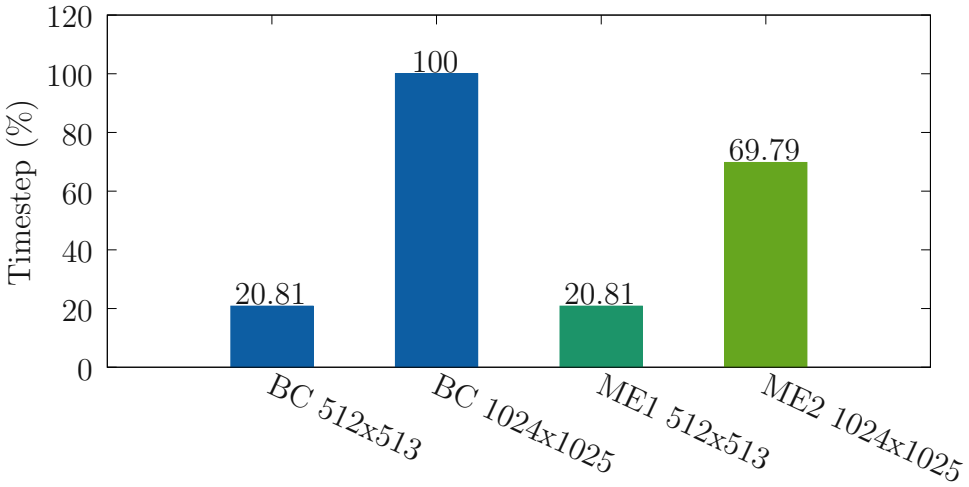

Figure 3.12 – Time comparison - Marconi 100 - (NYCPU=1, NZCPU=64)

Conclusion

These results emphasize the importance of the multiple-grid approach implemented for the phase-field. When the Navier-Stokes equations are already resolved on the Kolmogorov scale, we can save up to 30% in time, hard disk space and memory (RAM) for 2D simulations when only the Cahn-Hillard equation is expanded by a factor of 2 instead of the whole set of equations (2.12,2.13 and 2.14) is expanded.

3.2 Thin sheet layer break-up - 3D Benchmark

For the 3D benchmark, a thin sheet layer ($\phi = +1$, thickness=$0.15\tilde{h}$) is placed in the center of the channel, as shown in the figures (3.13, 3.14). A fully developed turbulent flow is initialized at the beginning. Therefore, the further developed code will be benchmarked and compared against the previous code, where the same conditions apply for the phase-field in both cases. In this benchmark, the mass losses, the bulk Reynolds number Re_{bulk}, a visual comparison of the phase-fields and the corresponding velocity profiles are compared. Last but not least, a time and memory comparison is done on the internal server S21.

3.2.1 Problem definition

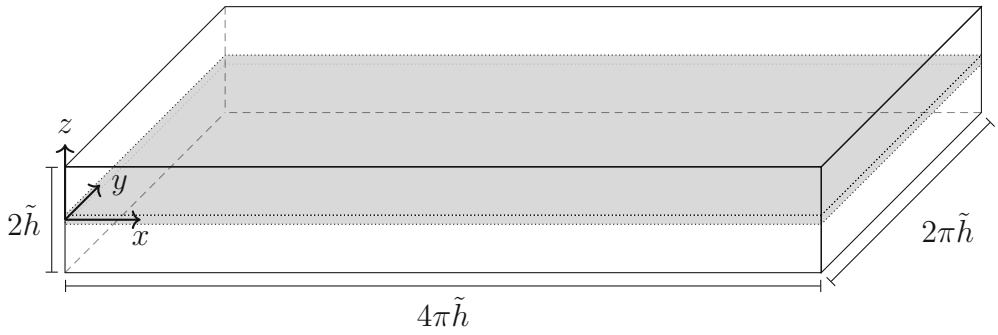

Figure 3.13 – Channel geometry used in the simulations. The channel is periodic in x- and y-directions and has respective lengths $\tilde{L}_x = 4\pi\tilde{h}$ and $\tilde{L}_y = 2\pi\tilde{h}$. Two walls are present along the z-axis and thus along the the wall-normal direction with a length in between of $\tilde{L}_z = 2\tilde{h}$

A thin sheet layer with a height of $0.15\tilde{h}$ is placed in the center of the simulated channel, as shown in figures (3.13, 3.14). The two walls are fixed and the velocity is driven by a pressure gradient, what is called a Poiseulle flow. Therefore, the simulation starts from turbulent initial fields, where the turbulent velocity profile is sketched in figure (3.14), and the Reynolds number is set to $Re_\tau = 150$. The three-dimensional computational domain is set to $\tilde{L}_x = 4\pi\tilde{h}$, $\tilde{L}_y = 2\pi\tilde{h}$ and $\tilde{L}_z = 2\tilde{h}$ in the corresponding directions and it has been discretized that the Navier-Stokes equations are resolved down to the Kolmogorov length scale. The Cahn number is always adopted to the discretization of the Cahn-Hillard equation, that there are at least 4 points for the interfacial transition layer, as mentioned in (§2.1.2), and the Peclet number is set as before to $Pe = 3/Ch$,

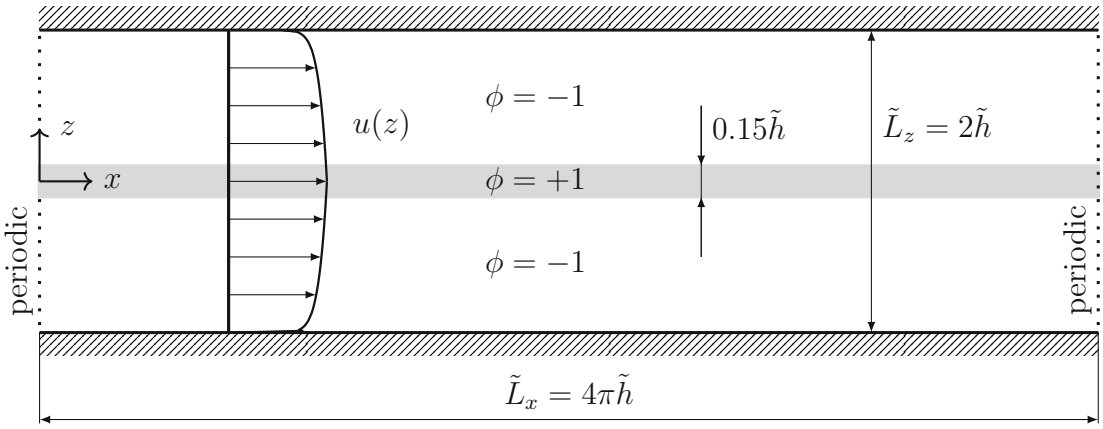

Figure 3.14 – Cross section at $y = 0$; Fully developed turbulent flow already at the beginning; In the center of the channel a thin sheet layer of a second fluid ($\phi = +1$, thickness $= 0.15\tilde{h}$) is inserted. A periodic boundary condition is applied on the left and on the right side.

see section (§2.2.3) or Magaletti et al. [21]. The density and viscosity ratios are set to $\lambda_\rho = \lambda_\eta = 1$ and last but not least, the Weber number is set to $We = 3$, leading to fast break-up of the thin layer.

3.2.2 Results

Mass loss and bulk Reynolds number $\mathbf{Re_{bulk}}$

Code	exp	Grid NSE	Grid CHE	Re	Ch	$\mathbf{Pe_\phi}$	We	Δt
BC	-	512x256x513	512x256x513	150	0.02	150	3	2.5e-5
ME2	2x2x2	256x128x257	512x256x513	150	0.02	150	3	2.5e-5

Table 3.3 – Overview of the simulations for the 3D benchmark;
BC . . . base code;
MEx . . . developed code with expansion factor x;

For all the benchmarks mentioned below, the following CPU core set-up is used. NYCPU = 8, where NYCPU represents the number of divisions of the domain for parallelization (y-direction in physical space, z-direction in modal space) and NZCPU = 12 (NZCPU . . . number of divisions of the domain for parallelization (z-direction when in physical space, y-direction when in modal space) where selected. In this first comparison, the mass losses (3.15a) and the bulk Reynolds number ($Re_{bulk} = \frac{u_{mean}}{u_\tau} Re_\tau$, shear velocity u_τ and shear Reynolds number Re_τ are already explained in chapter (2.2.3) and the mean velocity is shown in figure (3.17a)) (3.15b) are compared, where the mass losses are calculated by

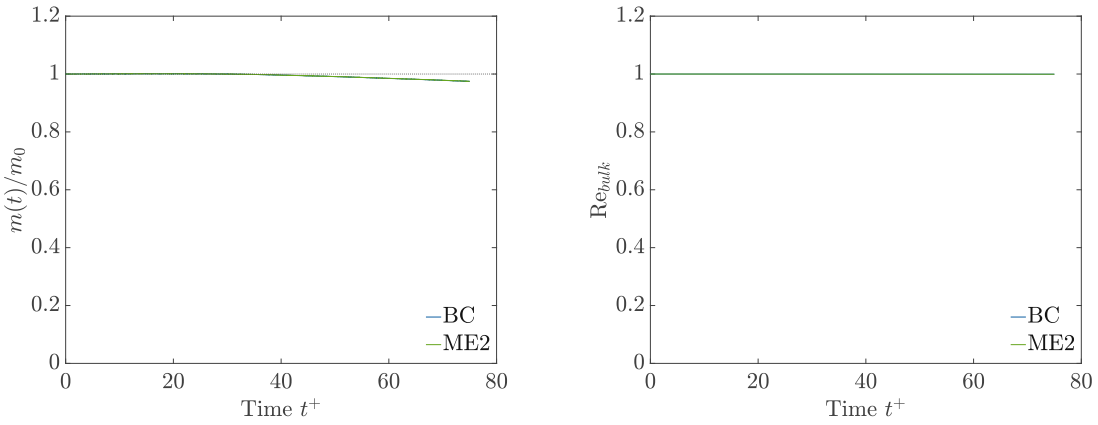

(a) Mass losses

(b) Re_{bulk}

Figure 3.15 – Figure a) shows the comparison of mass losses, where the dashed line indicates that there are no mass losses at all. Figure b) compares the bulk Reynolds number ($Re_{bulk} = \frac{u_{mean}}{u_\tau} Re_\tau$) of the two simulations.

integrating over the dispersed phase $\phi = +1$. The dashed line in the left plot for the mass losses, figure (3.15a), indicates that there are no mass losses at all ($\rightarrow \int \phi_{\phi=+1} = 1$). Both results indicate that there is no significant difference between these simulations, which shows that the same result will be obtained from the further developed and expanded code for the Cahn-Hillard equation (ME2-512x256x513) compared to the previous code (BC-512x256x513). Especially of interest is the 'Mass loss'-term because one can see directly that expanded code (ME2-512x256x513) delivers the same result as the previous one, since this mass losses depend on how fine the phase-field is resolved.

Visual comparison and velocity fields

For the visual comparison, the previously mentioned simulations (table (3.3)) have been compared. The simulation of the previous code (BC-512x256x513) compared to the multiple-grid approach (ME2-512x256x513) shows no evidence that the expansion of the phase-field has an influence on its solution, if the phase-field is resolved on the same grid in the end. Comparison of the front view (3.16a versus 3.16b) shows no difference at all. The blue area shows the carrier phase $\phi = -1$ and the red one corresponds to the dispersed phase $\phi = +1$. These figures (3.16a & 3.16b) are taken at $t^+ = 75$ and already indicate a deformed phase-field. The figures (3.16c & 3.16d) demonstrate the contour of the phase-field itself, also at the same t^+. One can see that

there are already a few holes and ligaments and even the first small drops are visible. Once again, no significant differences can be obtained from these graphs (3.16a-3.16d):

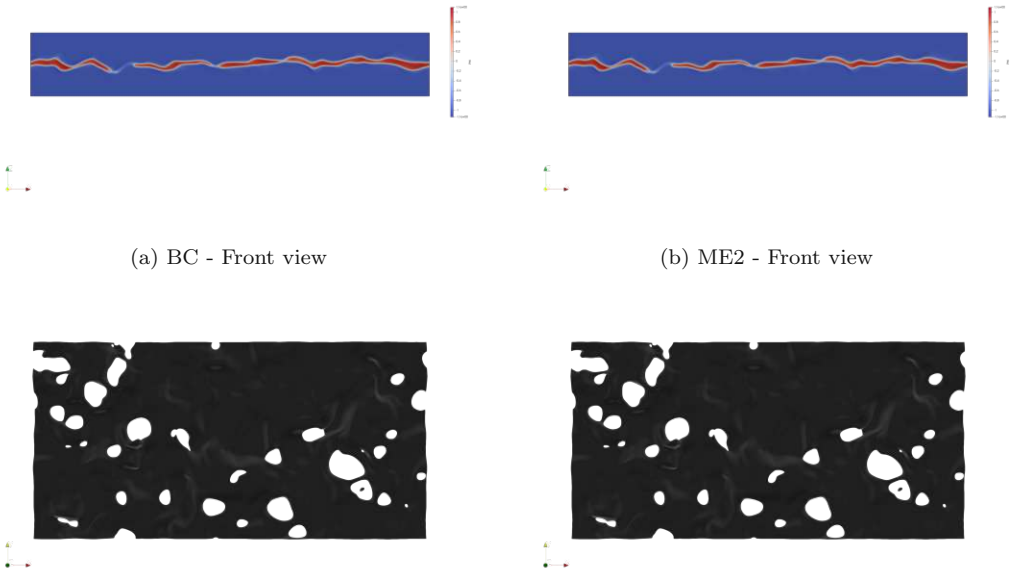

(a) BC - Front view

(b) ME2 - Front view

(c) BC - Top view

(d) ME2 - Top view

Figure 3.16 – Comparison of the current internal code BC and the further developed code ME2 after $t^+ = 75$; Figure a) & b) Shows the deformed thin sheet layer, where blue indicates the carrier phase ($\phi = -1$), gray indicates the interfacial transition layer and red indicates the dispersed phase($\phi = +1$)

Since the velocity in the streamwise direction is the dominating one, the u-velocities along the x-direction are compared in the figures (3.17a & 3.17b) at the same timestep. The average velocity $\vec{u}_{mean}$ shows the velocity profile and is needed to calculate the bulk Reynold number ($Re_{bulk} = \frac{u_{mean}}{u_\tau} Re_\tau$). In the plot (3.17a) the mean or average velocity profile is shown and computed as follows:

$$\vec{u}_{mean} = \frac{1}{N} \sum_{i}^{N} \vec{u} \tag{3.9}$$

In the figure next to (3.17b), the root-mean-square RMS velocity is illustrated and obtained as follows:

$$u_{rms} = \sqrt{\frac{1}{N} \sum_{i}^{N} |\vec{u}|^2} \tag{3.10}$$

The RMS velocity is important when the turbulent kinetic energy should be computed

and is always non-zero. And once again, neither for the average velocity (3.17a) nor for the root-mean-square velocity (3.17b) a significant difference is visible and the for the phase-field expanded code (ME2-512x256x513) delivers the same results for the phase as the previous not expanded one (BC-512x256x513).

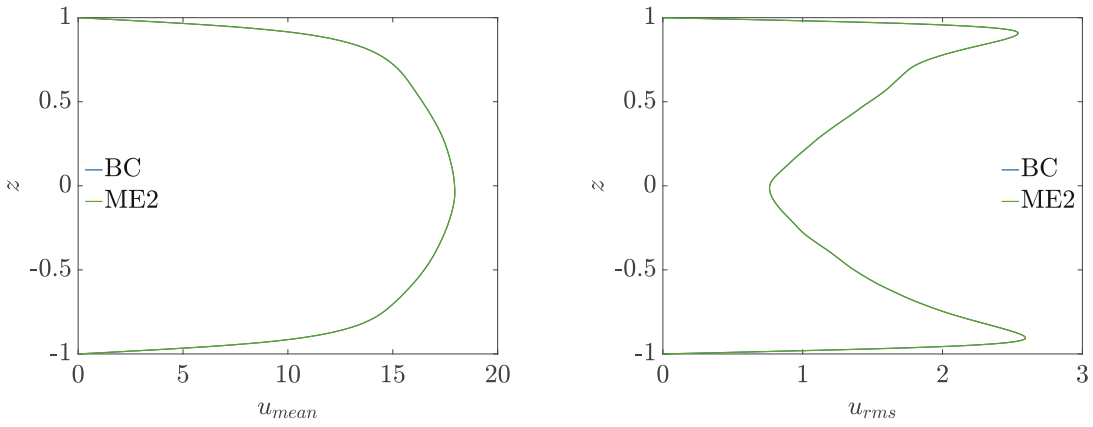

(a) Mean velocity

(b) RMS velocity in $x-$direction

Figure 3.17 – Velocity comparison after time $t^+ = 75$

Time and Memory comparison

Memory comparison

Code	exp	Grid NSE	Grid CHE	Re	Ch	Pe_ϕ	We	Δt
BC	-	512x256x513	512x256x513	150	0.02	150	3	2.5e-5
BC	-	1024x512x1025	1024x512x1025	150	0.01	300	3	2.5e-5
ME2	2x2x2	256x128x257	512x256x513	150	0.02	150	3	2.5e-5
ME4	4x4x4	256x128x257	1024x512x1025	150	0.01	300	3	2.5e-5

Table 3.4 – Overview of the simulations for the time and memory comparison;
BC ... base code;
MEx ... developed code with expansion factor x;

In this section, the time and memory savings of the 3D benchmark will be reviewed. The set-up of the CPU cores is still the same as mentioned before, with NYCPU=8 and NZCPU=12, so in total NYCPUxNZCPU=96 CPU cores are always used. The first comparison is (BC-512x256x513 versus ME2-512x256x513), where the grid used, in the newly developed code, for the Navier-Stokes equations can be halved

(Kolmogorov length scale still achieved) and the second one is (BC-1024x512x1025 versus ME4-1024x512x1025), where the grid is 64x(=4x4x4) smaller for the Navier-Stokes equations in the newly developed grid. In both comparisons for RAM (random-access memory), shown in the figure (3.18), it can be saved up to 50%. If you compare (BC-512x256x513 vs. BC-1024x512x1025), the increase in used RAM is dramatic, namely 7.62%. At this point, (ME4-1024x512x1025) can halve the RAM used for the same result in the end, which is an enormous win.

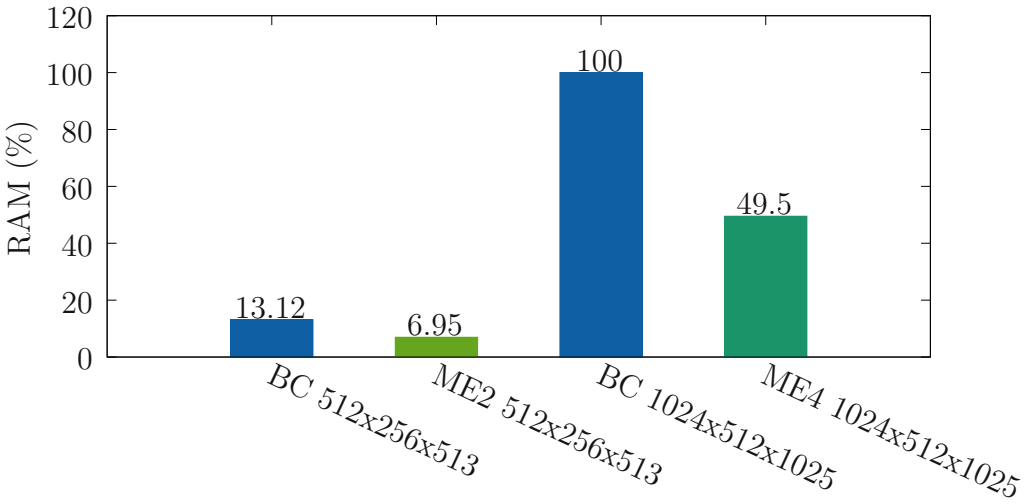

Figure 3.18 – Memory comparison - S21

Time comparison

The time comparison is obtained in the same way as for the 2D benchmark; for each of the four mentioned simulations in the table (3.4) five runs were performed and after 1000 timesteps, an estimate for the average time value was found for each simulation. After that, the average of the five simulations in total was obtained and used for this comparison. The comparison will be split into coarser and finer grids because the times are too different to obtain a usable comparison in the end. For the coarser grid, where the phase-field is expanded twice, while the Navier-Stokes equations are still solved on the Kolmogorov scale, the newly developed code (ME2-512x256x513) can save more than 30% in time compared to the current used internal code (BC-512x256x513), as seen in figure (3.19). If we keep the discretization for the Navier-Stokes equations and now expand all three directions by four instead of two (ME4-1024x512x1025)

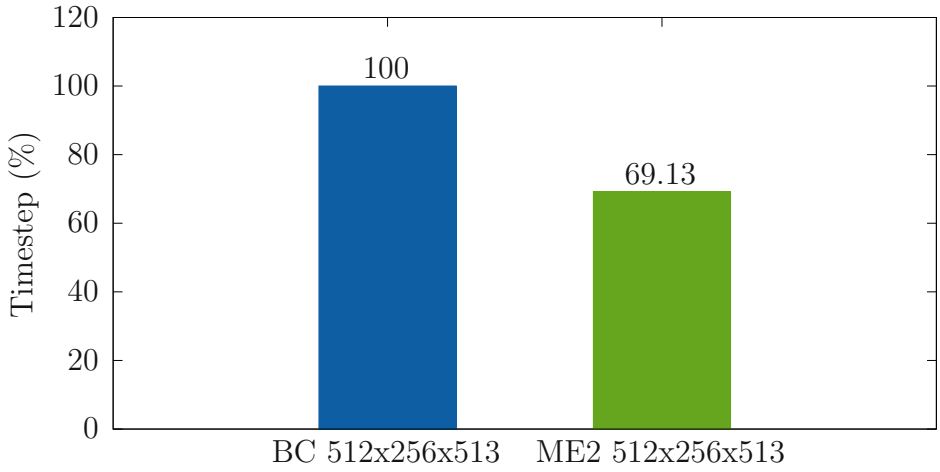

Figure 3.19 – Time comparison - S21 - Coarser grid

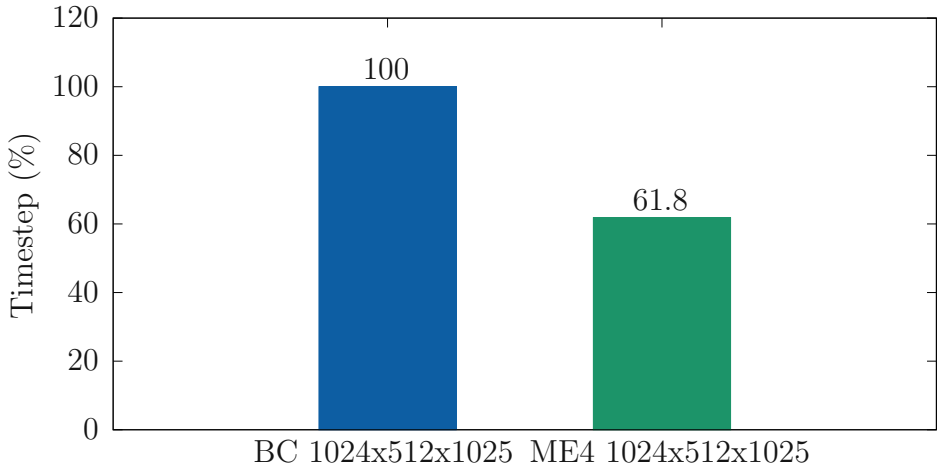

Figure 3.20 – Time comparison - S21 - Finer grid

and compare it with the current version of the internal code, where the Navier-Stokes equations will be overresolved again (BC-1024x512x1025), a time win for up to 40% can be achieved, as seen in figure (3.20).

Conclusion

The results of the 3D benchmark emphasizes the relevancy of the multiple-grid approach implemented for the Phase Field Method. As already seen for the 2D benchmark (§3.1), more than 40% can be saved in time and more than 50% in memory can be saved with this method by obtaining the same result in the end, when phase-field is resolved on the same grid.

4

Simulations

4.1 Thin sheet layer break-up

In this chapter, the main focus will be on how the mass and area over time t^+ develops and try to find some indications why they behave like this. For these simulations, almost the same set-up as for the 3D Benchmark is used again, where only the periodic lengths in $x-$ and $y-$directions are halved.

4.1.1 Problem definition

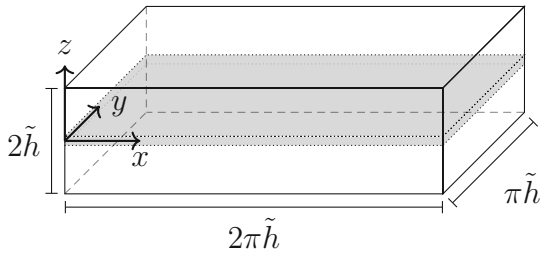

Figure 4.1 – Channel geometry used in the simulations. The channel is periodic in x- and y-directions and has respective lengths $\tilde{L}_x = 2\pi\tilde{h}$ and $\tilde{L}_y = \pi\tilde{h}$. Two walls are present along the z-axis and thus along the the wall-normal direction with a length in between of $\tilde{L}_z = 2\tilde{h}$

A thin sheet layer with a height of $0.15\tilde{h}$ is placed in the center of a simulated channel. The velocity is driven by a pressure gradient, and the two balls at the top and bottom are fixed, a so-called Poiseulle flow. The simulations start from turbulent initial fields, where the turbulent velocity profile is sketched in the figure (4.2) and the shear Reynolds number Re_τ=150. The three-dimensional computational domain is set to $\tilde{L}_x = 2\pi\tilde{h}$, $\tilde{L}_y = \pi\tilde{h}$ and $\tilde{L}_z = 2\tilde{h}$ in the corresponding directions, and it has been discretized that the Navier-Stokes equations are resolved down to the Kolmogorov length scale. For

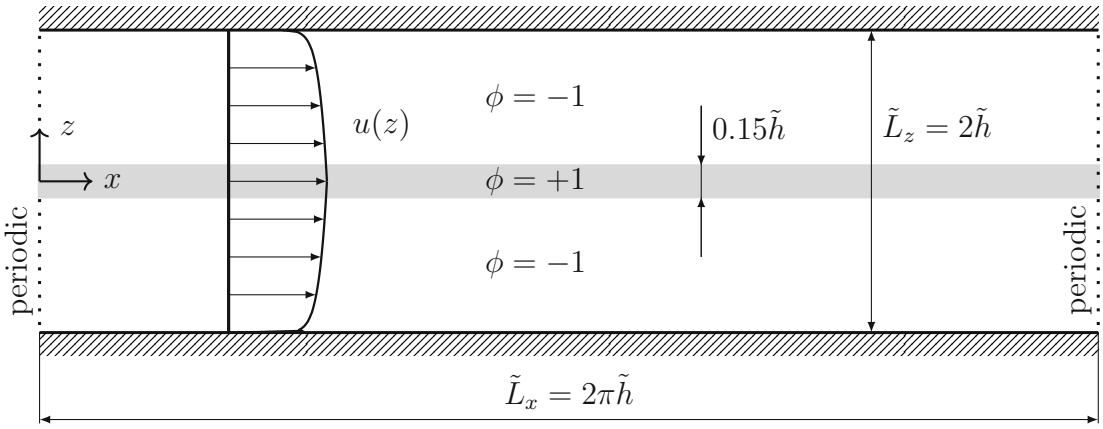

Figure 4.2 – Cross section at $y = 0$; Fully developed turbulent flow already at the beginning; In the center of the channel a thin sheet layer of a second fluid ($\phi = +1$, thickness $= 0.15\tilde{h}$) is inserted. A periodic boundary condition is applied on the left and on the right side.

the phase-field the Cahn number Ch is adapted for every simulation, so there are at least 4 grid points for the interfacial transition layer, as mentioned in (§2.1.2), and the Peclet number is set as before to $Pe = 3/Ch$, see section (§2.2.3) or Magaletti et al. [21]. The carrier and dispersed densities and viscosities match; therefore, the density and viscosity ratios are set to $\lambda_\rho = \lambda_\eta = 1$ and last but not least, the Weber number is set to $We = 3$, leading to fast break-up of the thin layer.

4.1.2 Results

Mass losses and surface area evolution

Code	exp	Grid NSE	Grid CHE	Re	Ch	Pe_ϕ	We	Δt
ME1	-	256x128x257	256x128x257	150	0.02	150	3	2.5e-5
ME2	2x2x2	256x128x257	512x256x513	150	0.01	150	3	2.5e-5
ME4	4x4x4	256x128x257	1024x512x1025	150	0.005	600	3	2.5e-5

Table 4.1 – Overview of the simulations for the time and memory comparison; MEx ... developed code with expansion factor x in both directions;

In this comparison, the main focus is on the mass losses of the Phase Field Method and the area evolution over time. In figure (4.3a), the mass losses for the three different simulations mentioned in table (4.1) are shown. A significant difference was found between these simulations. The correlation between mass leakages and the Cahn number

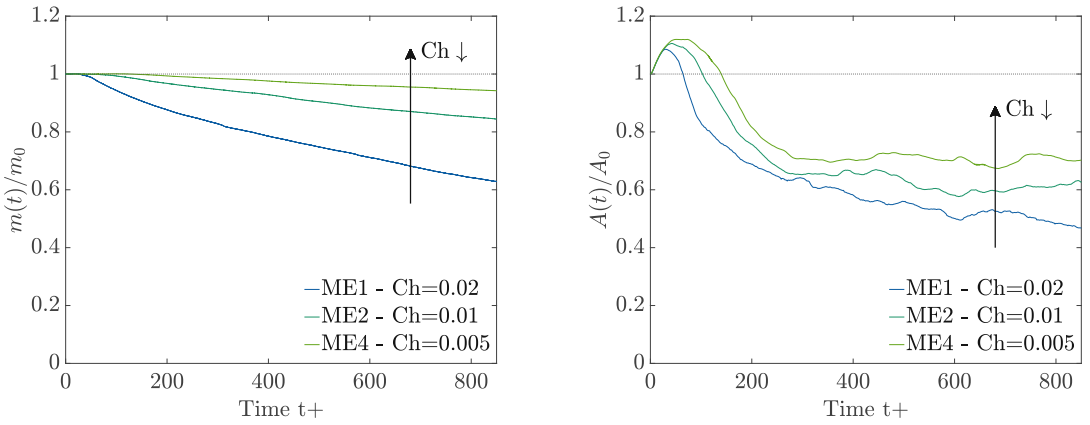

(a) Mass losses

(b) Surface area evolution

Figure 4.3 – Figure a) Shows the mass losses correlated to the Cahn number Ch; The dotted line indicates that there are no mass leakages at all; Figure b) Shows the surface area evolution correlated to the Cahn number

Ch is clearly recognizable. If the Cahn number Ch is reduced, the mass leakages also reduce significantly, where the dotted line in figure (4.3a) indicates that there are no mass losses at all. This substantiates the thesis; that the closer the phase-field is resolved to the molecular scale, the more mass leakages are reduced, since the resolution of the phase-field is proportional to the Cahn number Ch. Recall that there must always be at least four grid points to properly resolve the interfacial transition layer. To summarize: The finer the grid, the smaller the Cahn number Ch, resulting in less mass leakage in the end. The evolution of the surface area, figure (4.3b), follows the trend of mass leakages, with the result that by reducing the Cahn number Ch, there will be more surface area over time. The different curvatures of these lines in figure (4.3b) indicate something very interesting. First of all, the most noticeable is that all three curves rise in the beginning and after a certain amount of time, they start to fall more or less continuously. The surface area is normalized with the first entry, the starting point of the simulation. Therefore, the surface area grows before it finally starts to break-up. This phenomenon is shown in figure (4.4). In figure (4.4a), where the simulation (ME1-256x128x257) with Cahn number $Ch = 0.02$ is plotted, the tipping point is located at time $t^+ = 30$. Break-up starts slightly before the turnaround takes place and begins to dominate the development of the curve over the deformation of the thin sheet layer at the reverse point ($t^+ = 30$). The two red dots mark the surface area shortly before and after the tipping point. The first dot marks the time

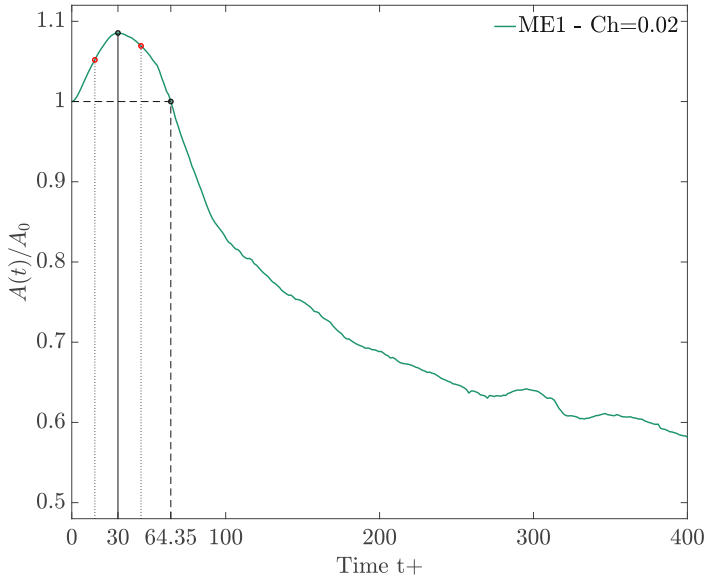

(a)

(b) $t^+ = 15$ (c) $t^+ = 45$

Figure 4.4 – Figure a) Shows the evolution of the surface area over time t^+; From the left: First red dot: $t^+ = 15$, First black dot: Tipping point at $t^+ = 30$, Second ret dot: $t^+ = 45$, Second black dot: Surface area equal to surface area at the beginning; Figure b) Phase-field contour at $t^+ = 15$; Figure c) Phase-field contour at $t^+ = 45$

$t^+ = 15$ and in the plot (4.4b), the deformed contour of the phase-field is shown. In plot (4.4c), which shows the second red dot at time $t^+ = 45$, the first holes and ligaments are already visible. To conclude this observation: Before the initial turbulent fields break the thin sheet layer, the thin layer will deform. Due to this deformation, the surface area will increase until the surface forces cannot keep them together, and the first holes and ligaments will form. After a time of $t^+ \sim 64.35$, the surface is smaller than it was at the beginning of the simulation (ME1-256x128x257). Furthermore, in figure (4.3b), when the grid is getting finer and the Cahn number Ch reduces, the tipping point delays in time and the maximum of the surface area grows. This indicates

that a finer resolution is capable of resolving the breakage and to the same extent the coalescence of droplets and ligaments can be reproduced even better.

4.1.3 Conclusion

In summary, these results show that the multiple-grid approach, where the phase-field can be expanded, mass leakages can be significantly reduced, and in addition, it also provides a more precise illustration of breakage and coalescence.

5

Conclusion

In this thesis, a mutliple-grid Phase Field Method approach is implemented and applied on a Direct Numerical Simulation DNS of a multiphase flow. The current internal code used was extended to decouple the grid of the Navier-Stokes equations, which corresponds to the momentum of the flow and, therefore, the velocity can be obtained from it, and the Cahn-Hillard equation, which takes care of the phase-field and describes which of the different mediums occurs where in the flow. This further developed code was tested and benchmarked mainly against the current code and for the 2D benchmark, also against an analytical solution. The 2D and 3D benchmarks have shown that keeping the Navier-Stokes equations finest needed scale, namely the Kolmogorov scale, and just pushing the phase-field on a finer grid can save a lot of time, memory and disk space, while the end result keeps the same. Pushing the phase-field on a finer grid allows us to reduce the Cahn number, which describes the ratio of the interface thickness to the used length scale in our simulated channel, and this procedure infers that the mass losses which occur for our chosen Phase Field Method will minimize proportional to the reduced Cahn number. To bring some numbers into play, the benchmarks have shown that more than 40% can be won in time and even up to 50% in memory (RAM - random-access memory) can be saved.

Bibliography

[1] D. M Anderson, G. B McFadden, and A. A Wheeler. DIFFUSE-INTERFACE METHODS IN FLUID MECHANICS. *Annual review of fluid mechanics*, 30(ISSN: 0066-4189):165, 1998. Place: Palo Alto, CA 94303-0139 Publisher: Palo Alto, CA 94303-0139: Annual Reviews.

[2] UM ASCHER, SJ RUUTH, and BTR WETTON. Implicit-Explicit Methods for Time-Dependent Partial Differential Equations. *SIAM journal on numerical analysis*, 32(3):797–823, 1995. Place: PHILADELPHIA Publisher: Society for Industrial and Applied Mathematics.

[3] V.E Badalassi, H.D Ceniceros, and S Banerjee. Computation of multiphase systems with phase field models. *Journal of computational physics*, 190(ISSN: 0021-9991):397, 2003. Place: SAN DIEGO Publisher: SAN DIEGO: Elsevier Inc.

[4] G. K Batchelor. *An Introduction to Fluid Dynamics*. Cambridge mathematical library. Cambridge University Press, New York, 2000.

[5] John Philip Boyd. *Chebyshev & Fourier spectral methods*. Lecture notes in engineering. Springer, Berlin [u.a.], 1989.

[6] John W. Cahn. Free energy of a nonuniform system. II. Thermodynamic basis. *The Journal of chemical physics*, 30(ISSN: 0021-9606):1124, 1959.

[7] John W. Cahn and John E. Hilliard. Free energy of a nonuniform system. I. Interfacial free energy. *The Journal of chemical physics*, 28(ISSN: 0021-9606):267, 1958.

[8] John W. Cahn and John E. Hilliard. Free energy of a nonuniform system. III. Nucleation in a two-component incompressible fluid. *The Journal of chemical physics*, 31(ISSN: 0021-9606):699, 1959.

[9] Bing Dai and L. Gary Leal. The mechanism of surfactant effects on drop coalescence. *Physics of fluids (1994)*, 20(ISSN: 1070-6631):040802–13, 2008. Place: MELVILLE Publisher: MELVILLE: American Institute of Physics.

[10] Wellington C de Jesus, Alexandre M Roma, Márcio R Pivello, Millena M Villar, and Aristeu da Silveira-Neto. A 3D front-tracking approach for simulation of a two-phase fluid with insoluble surfactant. *Journal of computational physics*, 281(ISSN: 0021-9991):420, 2015. Place: SAN DIEGO Publisher: SAN DIEGO: Elsevier Inc.

[11] C.W. Hirt and B.D. Nicholos. Volume of fluid (VOF) method for the dynamics of free boundaries. *J. Comput. Phys.*, 39(1):201–225, 1981.

[12] M Y Hussaini and T A Zang. Spectral Methods in Fluid Dynamics. *Annual review of fluid mechanics*, 19(1):339–367, 1987. Place: Palo Alto, CA 94303-0139 Publisher: Annual Reviews.

[13] t. Inamuro, R. Tomita, and F. Ogino. Lattice Boltzmann simulations of drop deformation and breakup in shear flows. *International journal of modern physics*, 17:21, 2003. Place: Singapore [u.a.] Publisher: World Scientific.

[14] David Jacqmin. Calculation of Two-Phase Navier–Stokes Flows Using Phase-Field Modeling. *Journal of computational physics*, 155(ISSN: 0021-9991):127, 1999. Place: SAN DIEGO Publisher: SAN DIEGO: Elsevier Inc.

[15] John Kim, Parviz Moin, and Robert Moser. Turbulence statistics in fully developed channel flow at low Reynolds number. *Journal of fluid mechanics*, 177:133–166, 1987. Place: Cambridge, UK Publisher: Cambridge University Press.

[16] A.E. Komrakova, Orest Shardt, D. Eskin, and J.J. Derksen. Lattice Boltzmann simulations of drop deformation and breakup in shear flow. *International journal of multiphase flow*, 59:24–43, 2014. Place: OXFORD Publisher: Elsevier Ltd.

[17] Ming-Chih Lai, Yu-Hau Tseng, and Huaxiong Huang. An immersed boundary method for interfacial flows with insoluble surfactant. *Journal of computational physics*, 227(ISSN: 0021-9991):7293, 2008. Place: SAN DIEGO Publisher: SAN DIEGO: Elsevier Inc.

[18] V. G. Levich. Physicochemical Hydrodynamics. *American Journal of Physics*, 31(11):892–892, 1963. _eprint: https://doi.org/10.1119/1.1969158.

[19] Fang-Hua Lin and Chun Liu. Nonparabolic dissipative systems modeling the flow of liquid crystals. *Communications on pure and applied mathematics*, 48(5):501–537, 1995. Place: New York Publisher: Wiley Subscription Services, Inc., A Wiley Company.

[20] Hao-Ran Liu and Hang Ding. A diffuse-interface immersed-boundary method for two-dimensional simulation of flows with moving contact lines on curved substrates. *Journal of computational physics*, 294(ISSN: 0021-9991):502, 2015. Place: SAN DIEGO Publisher: SAN DIEGO: Elsevier Inc.

[21] F Magaletti, F Picano, M Chinappi, L Marino, and C. M Casciola. The sharp-interface limit of the Cahn–Hilliard/Navier–Stokes model for binary fluids. *Journal of fluid mechanics*, 714:95–126, 2013. Place: Cambridge, UK Publisher: Cambridge University Press.

[22] Metin Muradoglu and Gretar Tryggvason. Simulations of soluble surfactants in 3D multiphase flow. *Journal of computational physics*, 274(ISSN: 0021-9991):757, 2014. Place: SAN DIEGO Publisher: SAN DIEGO: Elsevier Inc.

[23] R. Ostilla-Monico, Yantao Yang, E.P. van der Poel, D. Lohse, and R. Verzicco. A multiple-resolution strategy for Direct Numerical Simulation of scalar turbulence. *Journal of computational physics*, 301:308–321, 2015. Place: SAN DIEGO Publisher: Elsevier Inc.

[24] Swapna S Rabha and Vivek V Buwa. Volume-of-fluid (VOF) simulations of rise of single/multiple bubbles in sheared liquids. *Chemical engineering science*, 65(ISSN: 0009-2509):537, 2010. Place: Kidlington Publisher: Kidlington: Elsevier Ltd.

[25] J M Rallison. The Deformation of Small Viscous Drops and Bubbles in Shear Flows. *Annual review of fluid mechanics*, 16(1):45–66, 1984. Place: Palo Alto, CA 94303-0139 Publisher: Annual Reviews.

[26] Alessio Roccon. *Direct numerical simulation of turbulence-interface interactions*. PhD thesis, University of Udine, Udine, 2017.

[27] Alessio Roccon. Physics and high-performance computation of turbulent flows with interfaces, February 2020.

[28] J. A Sethian and Peter Smereka. LEVEL SET METHODS FOR FLUID INTERFACES. *Annual review of fluid mechanics*, 35(1):341–372, 2003. Place: Palo Alto, CA 94303-0139 Publisher: Annual Reviews.

[29] M. Shapira and S. Haber. Low Reynolds number motion of a droplet in shear flow including wall effects. *International Journal of Multiphase Flow*, 16(2):305–321, 1990.

[30] Giovanni Soligo. *Numerical simulations of breakage, coalescence and droplet size distribution*. PhD thesis, Vienna University of Technology, Wien, 2020. Journal Abbreviation: Numerical simulations of Publication Title: Numerical simulations of.

[31] Giovanni Soligo, Alessio Roccon, and Alfredo Soldati. Breakage, coalescence and size distribution of surfactant-laden droplets in turbulent flow. *Journal of fluid mechanics*, 881(ISSN: 0022-1120):282, 2019.

[32] Giovanni Soligo, Alessio Roccon, and Alfredo Soldati. Turbulent Flows With Drops and Bubbles: What Numerical Simulations Can Tell Us—Freeman Scholar Lecture. *Journal of fluids engineering*, 143(8), 2021. Place: NEW YORK Publisher: ASME.

[33] H. A Stone and L. G Leal. The effects of surfactants on drop deformation and breakup. *J. Fluid Mech*, 220(ISSN: 0022-1120):186, 1990. Place: Cambridge, UK Publisher: Cambridge, UK: Cambridge University Press.

[34] Geoffrey Ingram Taylor. The viscosity of a fluid containing small drops of another fluid. *Proceedings of the Royal Society of London. Series A, Containing papers of a mathematical and physical character*, 138(834):41–48, 1932. Place: London Publisher: The Royal Society.

[35] Geoffrey Ingram Taylor. The formation of emulsions in definable fields of flow. *Proceedings of the Royal Society of London. Series A, Containing papers of a mathematical and physical character*, 146(858):501–523, 1934. Place: London Publisher: The Royal Society.

[36] Gyula I. Tóth and Bjørn Kvamme. Analysis of Ginzburg-Landau-type models of surfactant-assisted liquid phase separation. *Phys Rev E Stat Nonlin Soft Matter Phys*, 91(ISSN: 1539-3755):032404, 2015. Place: COLLEGE PK Publisher: COLLEGE PK: Amer Physical Soc.

[37] J.D. van der Waals. The thermodynamic theory of capillarity under the hypothesis of a continuous variation of density. *Journal of statistical physics*, 20(2):200–244, 1979.

[38] N. P van Dijk, K Maute, M Langelaar, and F van Keulen. Level-set methods for structural topology optimization: a review. *Structural and multidisciplinary optimization*, 48(3):437–472, 2013. Place: Berlin/Heidelberg Publisher: Springer Berlin Heidelberg.

[39] PENGTAO YUE, JAMES J FENG, CHUN LIU, and JIE SHEN. A diffuse-interface method for simulating two-phase flows of complex fluids. *Journal of fluid mechanics*, 515:293–317, 2004. Place: Cambridge, UK Publisher: Cambridge University Press.

List of Figures

List of Tables